Origins of large-volume, compositionally zoned volcanic eruptions: New constraints from U-series isotopes and numerical thermal modeling for the 1912 Katmai-Novarupta eruption

Simon Turner,[1] Mike Sandiford,[2] Mark Reagan,[3] Chris Hawkesworth,[4] and Wes Hildreth[5]

Received 8 December 2009; revised 11 June 2010; accepted 1 July 2010; published 1 December 2010.

[1] We present the results of a combined U-series isotope and numerical modeling study of the 1912 Katmai-Novarupta eruption in Alaska. A stratigraphically constrained set of samples have compositions that range from basalt through basaltic andesite, andesite, dacite, and rhyolite. The major and trace element range can be modeled by 80–90% closed-system crystal fractionation over a temperature interval from 1279°C to 719°C at 100 MPa, with an implied volume of parental basalt of ~65 km^3. Numerical models suggest, for wall rock temperatures appropriate to this depth, that 90% of this volume of magma would cool and crystallize over this temperature interval within a few tens of kiloyears. However, the range in $^{87}Sr/^{86}Sr$, ($^{230}Th/^{238}U$), and ($^{226}Ra/^{230}Th$) requires open-system processes. Assimilation of the host sediments can replicate the range of Sr isotopes. The variation of ($^{226}Ra/^{230}Th$) ratios in the basalt to andesite compositional range requires that these were generated less than several thousand years before eruption. Residence times for dacites are close to 8000 years, whereas the rhyolites appear to be 50–200 kyr old. Thus, the magmas that erupted within only 60 h had a wide range of crustal residence times. Nevertheless, they were emplaced in the same thermal regime and evolved along similar liquid lines of descent from parental magmas with similar compositions. The system was built progressively with multiple inputs providing both mass and heat, some of which led to thawing of older silicic material that provided much of the rhyolite.

Citation: Turner, S., M. Sandiford, M. Reagan, C. Hawkesworth, and W. Hildreth (2010), Origins of large-volume, compositionally zoned volcanic eruptions: New constraints from U-series isotopes and numerical thermal modeling for the 1912 Katmai-Novarupta eruption, *J. Geophys. Res.*, *115*, B12201, doi:10.1029/2009JB007195.

1. Introduction

[2] Volcanoes provide a visually stunning testament to the existence of the Earth′s thermal engine, and there is joint public and scientific interest in volcanoes, both as a natural hazard and as a window into the primary mechanism of the Earth′s differentiation. Large-volume, caldera-forming, high-silica, pyroclastic rhyolites are the most destructive volcanic eruptions on Earth. They typically erupt at high temperatures and emit large volumes of H_2O, H_2S, SO_2 and CO_2 that have a demonstrable influence on global climate [*Robock and Mao*, 1992]. The high SiO_2 and volatile contents in these eruptions suggest these magmas represent the products of extended magmatic differentiation, yet exactly how such large and potentially explosive magma volumes are formed remains enigmatic. Several decades of field and fluid dynamic research [e.g., *Turner and Campbell*, 1986] have identified three increasingly well-defined models: the evacuation of long-lived, zoned magma chambers [*Hildreth*, 1981] generated largely by crystal fractionation [*Bacon and Druitt*, 1988]; the re-melting of granitic plutons by intrusion of basaltic magmas [*Huppert and Sparks*, 1988]; and the shallow-level interaction of magmas of contrasting composition just prior to eruption [*Eichelberger and Izbekov*, 2000]. More recently, *Annen et al.* [2006] have considered the extent to which injection of basalt combined with partial melting and mixing in the lower crust might produce intermediate and silicic magmas. *Price et al.* [2005] and *Reubi and Blundy* [2009] have also argued that intermediate composition magmas in many systems reflect mixing between mafic and silicic melts. All these models differ in the predicted relations between different magma types, and in the time scales of magma formation and residence underground. Thus, short-lived (U-series) isotopes and numerical thermal models, combined with the results of detailed field work, provide an opportunity to now test these models in ways that

[1]GEMOC, Department of Earth and Planetary Sciences, Macquarie University, North Ryde, New South Wales, Australia.
[2]School of Earth Sciences, University of Melbourne, Parkville, Victoria, Australia.
[3]Department of Geoscience, University of Iowa, Iowa City, Iowa, USA.
[4]Department of Earth Sciences, University of Bristol, Bristol, UK.
[5]United States Geological Survey, Menlo Park, California, USA.

0148-0227/10/2009JB007195

were less possible when they were originally proposed. Quantifying the rates of magma build-up may provide useful insights into present preeruptive conditions that may aid predictions of future volcanic activity.

[3] Our knowledge of the processes that occur in magma chambers stems largely from the study of their erupted volcanic products, since plutons provide, at best, only a time-integrated view of the solidified remains of magma chambers [e.g., *Brown and Rushmer*, 2006]. In particular, the zoned deposits of large pyroclastic eruptions and the inference that these deposits represent the inverted stratigraphy of underlying magma chambers have been the basis for models in which magma chambers develop compositional layering. Most notably, *Hildreth* [1981] presented evidence that these deposits could be derived from long-lived, thermally and compositionally stratified magma chambers maintained and fed from below by mantle-derived magmas. The notion of long-lived, layered magma chambers has become somewhat of a paradigm extrapolated to many zoned, pyroclastic deposits.

[4] Radiogenic isotopes and trace element ratios have been widely used to distinguish comagmatic suites. However, with the addition of U-series isotope analyses it is now possible to distinguish magmas that may have similar bulk compositions but different ages on time scales of 10^2–10^5 years [e.g., *Hawkesworth et al.*, 2000]. This offers the opportunity of exciting new insights into the dynamics of magma systems from the variations in composition and preeruption ages within zoned eruptive units. The increasing sophistication of numerical models has also highlighted that a key discriminator of the different models is the predicted timescale of magma formation and residence underground. Zoned magma chambers tens to hundreds of square kilometers in size require 10^4–10^5 years to form and become stratified in a stable manner [*Trial and Spera*, 1990; *Wolff et al.*, 1990]. Once stratified, the chambers could, in theory, remain unmixed for 10^5–10^6 years [*Oldenburg et al.*, 1989]. However, such models require particular thermal conditions, since pluton-sized bodies will also cool on a time scale of 10^4–10^5 years [*Spera*, 1980]. Remelting of preexisting granitic plutons, on the other hand, is predicted to occur on markedly shorter time scales of 10^2–10^3 years [*Huppert and Sparks*, 1988], and in this model the more mafic magmas are likely to have contrasting trace element and isotope signatures. More controversially, it has been suggested that some zoned, high-silica eruptions reflect the injection of rhyolite into an andesitic magma chamber [*Eichelberger and Izbekov*, 2000], in which case the silicic magma could have a shorter crustal residence time than the andesite with no genetic link predicted between them. Finally, the "hot zone" model predicts incubation over 0.1–10 Myr with little U-series disequilibria predicted unless the melts contain significant recent contributions from the mantle [*Annen et al.*, 2006].

[5] Much of the debate has centered around the interpretation of controversial long residence times inferred for high-silica magmas at Long Valley where Rb-Sr isochron evidence for magma residence times of up to 0.7 Myr seemed to strongly support the long-lived chamber paradigm [*Halliday et al.*, 1989]. However, *Sparks et al.* [1990] strongly questioned the interpretation of these isochrons, invoking instead the remelting of 0.7 Ma plutons sometime in the previous few hundreds to thousands of years [*Huppert and Sparks*, 1988]. This ongoing controversy has led to numerous attempts to verify the residence times of the Long Valley high-silica magmas and the development of some intermediate models [*Halliday et al.*, 1989; *Sparks et al.*, 1990; *van den Bogaard and Schirnick*, 1995; *Davies and Halliday*, 1998; *Christensen and DePaolo*, 1993; *Mahood*, 1990; *Hildreth and Wilson*, 2007]. However, the compositional range of the deposits studied at Long Valley does not include more primitive rocks that could be the parental magmas in the zoned magma chamber model, the heat source in the re-melting model, or the resident magma in the shallow interaction model. Moreover, these rocks are too old for short-lived U-series isotope studies and the only natural laboratory of a zoned magmatic system in which the full complement of radiogenic isotopes, numerical predictions and U-series isotopes can be applied is the Katmai-Novarupta eruption of 1912.

[6] Accordingly, we have undertaken an integrated radiogenic and U-series isotope and numerical thermal modeling study of a stratigraphically constrained section through the Katmai-Novarupta deposits. Clasts of andesite, dacite and rhyolite are present at most stratigraphic levels [*Hildreth and Fierstein*, 2000] and these were individually analyzed to investigate the scale of temporal variations in the magmas prior to eruption and the time scales over which they are interrelated.

2. The Katmai-Novarupta 1912 Eruption

[7] In June 1912, the biggest and one of the most compositionally diverse eruptions of the last century took place in the Katmai group of volcanoes on the Alaska Peninsula (Figure 1). In the space of 60 h, 13 km^3 of rhyolite, dacite, and andesite magma were explosively ejected, producing an ash cloud covering 77,000 km^2 that extended as far east as Greece and filled the Valley of Ten Thousand Smokes. The eruption was larger than the 1883 Krakatau eruption, releasing more HCl than Mount St. Helens in 1980, as much H_2SO_4 as the Minoan eruption of Santorini, and producing 250 times more seismic energy than Pinatubo in 1991 [*Westrich et al.*, 1991; *Hildreth and Fierstein*, 2000]. The Pinatubo eruption reduced northern hemisphere temperatures by 0.2°C, having a similar effect to that of El Niño [*Rampino and Self*, 1984]. Although the eruption took place from a vent at the site of the present-day Novarupta dome (Figure 1), it involved lateral magma transport from the summit of Mount Katmai, 10 km to the east, which started to collapse some 11 h after the onset of the eruption to form a 5.5 km^3 caldera [*Hildreth and Fierstein*, 2000].

[8] Detailed stratigraphic studies by *Fierstein and Hildreth* [1992] and *Fierstein and Wilson* [2005] have divided the eruption into three main episodes. During episode 1 (8.8 km^3), the onset of the eruption was marked by the plinian dispersal of 3 km^3 of high-silica, crystal-poor rhyolitic magma (layer A). This was followed by a gradual increase in the proportions of dacitic and andesitic material (layer B), leading to a progressive shift from bulk rhyolite pumice through to andesite scoria in the resulting zoned ignimbrite sheet emplaced in the Valley of the Ten Thousand Smokes. Episode 2 (4.8 km^3) began after a brief lull with a plinian eruption of more phenocryst-rich andesite and dacite (layers C and D). Subordinate rhyolite was deposited in the

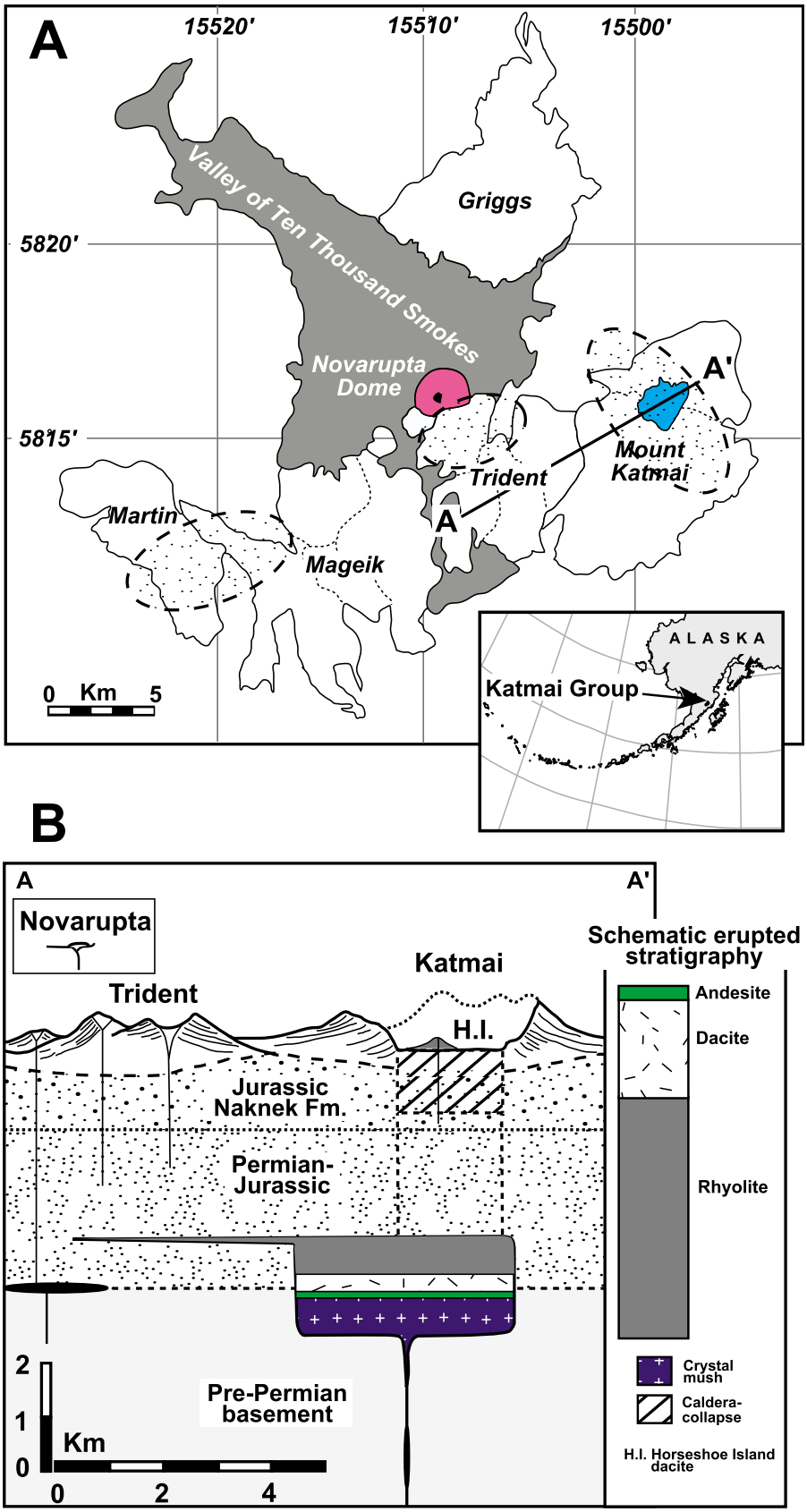

Figure 1. (a) Map of the Katmai volcanic cluster with inset showing location on the Alaskan Peninsula. (b) Schematic cross section of region A-A′ in Figure 1a [after *Hildreth and Fierstein*, 2000].

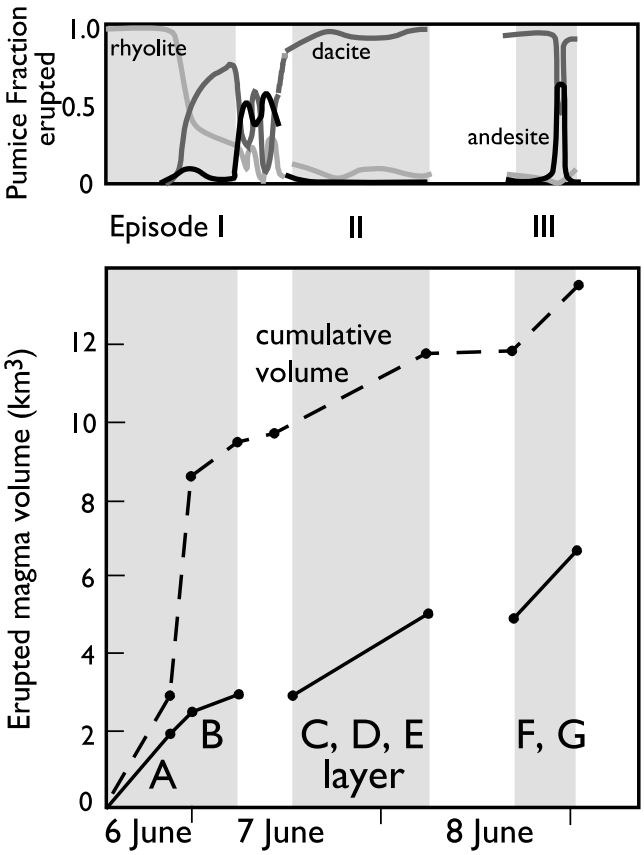

Figure 2. Stratigraphy of the 1912 eruption showing the division of the various layers into three eruptive episodes [after *Fierstein and Hildreth*, 1992].

lower part of layer C but was very sparse thereafter. After another brief lull, episode 3 (3.4 km^3) deposited plinian dacite layers F and G. Layer H is a postplinian ashfall deposit. Figure 2 illustrates how the proportions of rhyolitic (55%), dacitic (35%), and andesitic (10%) clasts changed systematically during the eruption. The total 17 km^3 of fall deposits correspond to ~13 km^3 of magma [*Fierstein and Wilson*, 2005].

[9] Previous activity in the area dominantly involved Holocene andesitic magmatism [*Hildreth and Fierstein*, 2000] down to 2.5 ka, suggesting that it may have taken at least a couple of thousand years to develop the 8 km^3 of volatile-rich, high-silica rhyolite which is unique to the 1912 eruption. The crystal-poor nature of the high-silica rhyolite is striking, and one interpretation is that it was a residual liquid extruded from an andesite-dacite mush [*Hildreth and Fierstein*, 2000]. Degassing might have been restricted by eruption through relatively impermeable Naknek Formation sediments, leading to the explosive nature of the eruption. All other eruptions in the area occurred through rocks of higher permeability and by contrast were largely effusive [*Hildreth and Fierstein*, 2000].

[10] As summarized by *Hildreth* [1983], the andesites and dacites are 30–50% composed of phenocrysts of plagioclase, orthopyroxene, augite, and oxides in the proportions 5:2:1:1, with minor olivine found in some andesite clasts. In contrast, the rhyolites are 1–3% composed of phenocrysts of quartz, plagioclase, orthopyroxene, and opaques in the proportions 5:5:2:1. Overall, the SiO_2 contents of the clasts range discontinuously from 50 wt %–77 wt %, with a silica gap that is 68 wt %–76 wt % SiO_2. However, the continuous variation in Fe-Ti oxide temperatures and redox in the three magma types (Figure 3) led *Hildreth* [1983] to suggest that the zoned eruption had been fed by a single, layered magma chamber beneath Katmai. Moreover, interstitial glass in the andesite is similar to the composition of the bulk dacite, and the glass in the dacite is nearly identical to the bulk rhyolite. However, there is no evidence that the dacite reflects mixing between the rhyolite and andesite end-members [*Hildreth and Fierstein*, 2000].

[11] Experimental work on erupted materials from the 1912 eruption suggests that under H_2O-saturated conditions the andesite and dacite were stored at 930°C –960°C and 100–75 MPa and 850°C–880°C and 50–25 MPa, respectively [*Hammer et al.*, 2002], while the rhyolite was held at 800°C–850°C at 100–40 MPa [*Coombs and Gardner*, 2001]. Thus, magma storage was at very shallow depths (1–5 km) before eruption. However, if all three magmas were H_2O-saturated, then the rhyolite would have resided deeper and thus would have been laterally displaced from the andesite and dacite [*Coombs and Gardner*, 2001; *Hammer et al.*, 2002]. Alternately, if the andesite and dacite were H_2O-undersaturated, it is possible that all three magmas coexisted in a single vertically zoned magma chamber [*Coombs and Gardner*, 2001; *Hammer et al.*, 2002]. This is consistent with the model proposed by *Hildreth and Fierstein* [2000] having an elongate flattened chamber, 1.3 km deep, 2 km across, and 5 km long, holding 13 km^3 of erupted magma. This chamber was also inevitably underlain by an unknown volume of unerupted cumulate mush (Figure 1b).

[12] In previous U-series isotope work, *George et al.* [2003], *Reagan et al.* [2003], and *Turner et al.* [2004] have all presented preliminary U-series isotope data from some of the Katmai Group volcanics. *Reagan et al.* [2003] used U-Th isotope data to suggest that the generation of the Katmai rhyolite occurred by fractionation of andesite magma combined with assimilation of preexisting intrusives over $>10^5$ years. *Turner et al.* [2004] presented ^{210}Pb data from the 1958 eruptions of nearby Mount Trident that indicated

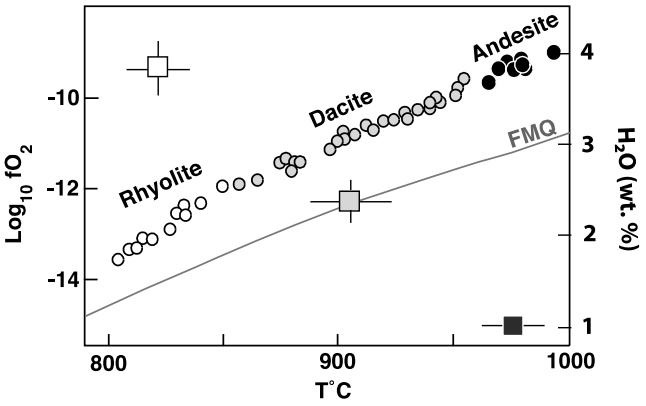

Figure 3. Oxygen fugacity and geothermometry data from the 1912 eruption [after *Hildreth*, 1983]. Water contents (squares) are from *Westrich et al.* [1991].

the presence of magma that had been undergoing shallow-level degassing for about a decade prior to eruption, and this is consistent with seismic evidence for the present-day presence of magma in the area [*Ward et al.*, 1991].

3. Sample Details and Analytical Techniques

[13] The majority of the 28 samples analyzed are a subset of a stratigraphically constrained suite for which major and trace element concentrations were previously determined using methods described elsewhere [e.g., *Fierstein and Hildreth*, 1992]. They include three near-vent scoria fall samples from the S bed described by *Fierstein et al.* [1997] and one sample from the lava dome at Novarupta. We also included a sample of the Naknek Formation sediments (sample AM23 from *Lowenstern and Mahood* [1991]) as a potential contaminant. Sr and U-Th-Ra isotopes were analyzed, either at the University of Bristol, following methods outlined by *George et al.* [2003], or at Macquarie University using the protocols described subsequently.

[14] At Macquarie University, Sr isotopic analyses used ~100 mg of powdered sample that was dissolved using HF-HNO_3 in a heated Teflon pressure bomb. Sr fractions were separated using a cationic column and loaded onto single Re filaments and analyzed in static mode on a ThermoFinnigan Triton® TIMS. Mass fractionation was corrected for by normalizing to $^{86}Sr/^{88}Sr = 0.1194$. Analyses of SRM987 and BHVO-2 performed at the same time yielded $^{87}Sr/^{86}Sr = 0.710287 \pm 25$ ($n = 4$) and 0.703496 ± 36 ($n = 7$), respectively.

[15] U, Th, and Ra concentrations and isotope ratios were determined on samples that were spiked with the same ^{226}U–^{229}Th and ^{228}Ra tracers used in Bristol and dissolved using an HF-HNO_3-HCl mix in heated Teflon pressure bombs. The product was converted to chloride using 6N HCl and then 6N HCl saturated with H_3BO_3 to remove residual fluorides. The final product was converted to nitrate using 14N HNO_3 and finally taken up in 7N HNO_3. U and Th purification was achieved via a single pass through a 4 ml anionic resin column using 7N HNO_3, 6N HCl and 0.2N HNO_3 as elutants. Concentrations and isotope ratios were measured in dynamic mode on an Nu Instruments® MC-ICP-MS at Macquarie University. ^{238}U and ^{235}U were analyzed on Faraday cups, using the $^{238}U/^{235}U$ ratio to determine the mass bias, assuming $^{238}U/^{235}U = 137.88$, while ^{236}U and ^{234}U were alternately collected in the IC0 ion counter that is equipped with a deceleration lens. The IC0 gain was determined during interspersed dynamic analyses of CRM145, assuming a $^{234}U/^{238}U$ ratio of 5.286×10^{-5} [*Cheng et al.*, 2000]. Methods for Th-isotope measurements employed a dynamic routine with ^{232}Th in Faraday cups and ^{230}Th and ^{229}Th alternating on IC0, as described in full detail in *Sims et al.* [2008]. Accuracy (<0.3%) and precision (<0.1%) were assessed by regular analyses of the U010 and ThA solution standards. Multiple analyses of the secular equilibrium rock standard TML-3 ($n = 5$) performed at the same time as the samples yielded the following results: U = 10.54 ppm, Th = 29.61 ppm, $(^{234}U/^{238}U) = 0.993$, $(^{230}Th/^{232}Th) = 1.088$, and $(^{230}Th/^{238}U) = 1.007$; these results are within the error of secular equilibrium and published values for this rock [*Sims et al.*, 2008].

[16] Ra was taken from the first elution from the anionic column and converted to chloride using 6N HCl. This was then loaded in 3N HCl onto an 8 ml cationic column and eluted using 3.75M HNO_3 and the process repeated on a scaled-down 0.6 ml column. Ra and Ba were then chromatographically separated using ElChrom® Sr-spec resin™ and 3N HNO_3 as elutant in a 150 μl procedure. Samples were loaded onto degassed Re filaments using a Ta-HF-H_3PO_4 activator solution, and $^{228}Ra/^{226}Ra$ ratios were measured to a precision typically ~0.5% in dynamic ion counting mode on a ThermoFinnigan Triton® TIMS at Macquarie University. Organic interferences often noted at low temperatures during TIMS analysis for Ra were eliminated by the purchasing of the instrument fitted with a dry scroll pump instead of the standard rotary pump, preventing leakage of organic molecules into the source during venting. Accuracy was assessed via replicate analyses ($n = 5$) of TML-3 that yielded $^{226}Ra = 3534$ fg/g and $(^{226}Ra/^{230}Th) = 1.002 \pm 0.008$ that is within error of secular equilibrium.

4. Results

[17] Complete data for the samples analyzed are presented in Table 1 and supplemented in some of the figures by data from basaltic andesite obtained from Novarupta dome (97ND02), as published by *George et al.* [2003], and data from another basaltic andesite (K851), as published by *Reagan et al.* [2003]. The samples range in SiO_2 from a single, nearly primitive basalt (50.4 wt % SiO_2 and 11.4 wt % MgO) and two basaltic andesites through the andesite-dacite continuum and across a silica gap (68 wt %–77 wt % SiO_2) to rhyolites that reach up to 77.7 wt % SiO_2 (Figure 4a). Over this silica range the corresponding MgO and FeO* contents decrease from 11.43 wt % to 0.02 wt % and 10.6 wt % to 1.3 wt %, respectively. CaO decreases and K_2O increases with decreasing MgO, whereas FeO* (Figure 4b) and Al_2O_3, Na_2O, and P_2O_5 (not shown) form curvilinear trends against MgO. Figure 4c shows that Al_2O_3 initially increases and then decreases with decreasing CaO. Across this compositional range, concentrations of compatible trace elements such as Sc decrease while incompatible element concentrations increase. In contrast, Ti, Zr, Sr, and Eu exhibit inflected trends that are initially increasing and then constant or decreasing in concentration with increasing SiO_2 (not shown). The overall incompatible trace element variation is illustrated on normalized incompatible element diagrams in Figure 5 which show a general parallelism and patterns typical of arc rocks from the Aleutians and elsewhere, with peaks in fluid-mobile elements (e.g., Ba, U, Sr, and Pb) and depletions in immobile elements such as Th, Nb, and Ti.

[18] Sr isotopes were measured on samples chosen to encompass the major element compositional range. The new $^{87}Sr/^{86}Sr$ data expand the previously reported restricted range [*Hildreth and Fierstein*, 2000] to 0.70339–0.70374, mainly because of the measurement of an $^{87}Sr/^{86}Sr$ ratio of 0.70339 in the basaltic scoria clast from the S bed. The range overlaps but is slightly smaller than the 0.70302–0.70388 variation reported for the present-day Aleutian arc in general [*George et al.*, 2003]. It is clear from a plot of $^{87}Sr/^{86}Sr$ versus SiO_2 that not all of the 1912 products can be interrelated by any simple liquid line of descent (Figure 6a). The Naknek sample was a sandstone with generally low incompatible element

Table 1. Geochemical and Isotopic Analyses From Katmai[a]

Sample #	Stratigraphy	SiO_2	TiO_2	Al_2O_3	FeO*	MnO	MgO	CaO	Na_2O	K_2O	P_2O_5	LOI	Total	Sc	Rb	Sr	Y	Zr	Nb	Cs	Ba	La	Ce	Pr
K1000a	layer A bottom	77.48	0.14	12.18	1.30	0.04	0.18	0.85	4.21	3.16	0.05	1.69	97.31	7.5	55.8	62	39.7	130	4.41	2.28	843	16.82	35.04	4.56
K1079a	layer A top	77.46	0.14	12.20	1.26	0.04	0.17	0.86	4.26	3.15	0.05	1.36	97.98	7.5	56.9	61	40.4	132	4.35	2.33	859	16.94	35.37	4.57
K2466b	layer B	59.64	0.73	16.70	6.76	0.13	3.59	7.16	3.41	1.31	0.17	0.34	98.58	28.2	25.7	298	25.2	106	3.50	1.00	417	9.77	20.54	2.75
K2488d	layer B	61.38	0.70	16.59	6.15	0.13	3.00	6.44	3.55	1.49	0.18	1.12	97.51	25.3	28.4	272	26.0	114	3.18	1.11	452	10.29	21.72	2.89
K0100c	main ignimbrite	64.02	0.68	15.69	5.57	0.12	2.51	5.31	3.93	1.61	0.15	1.24	98.08	19.6	26.9	254	27.1	120	3.10	1.07	460	10.27	21.90	2.90
K0121	main ignimbrite	77.70	0.13	12.11	1.25	0.04	0.16	0.86	4.11	3.20	0.05	2.80	96.27	6.8	53.8	58	37.3	122	3.94	3.02	794	15.71	32.64	4.19
K0135d	main ignimbrite	59.85	0.73	16.73	6.76	0.13	3.54	7.14	3.27	1.30	0.15	0.73	98.44	24.5	23.6	289	23.0	98	2.66	0.92	391	8.99	18.95	2.52
K0162	main ignimbrite	64.52	0.66	16.11	5.16	0.10	2.27	4.79	4.08	1.78	0.13	n.d.	98.24	17.4	33.6	232	30.8	142	3.73	1.37	550	11.98	25.33	3.37
K0182	main ignimbrite	65.52	0.67	15.77	5.03	0.09	2.11	4.56	3.91	1.80	0.13	n.d.	97.70	18.8	31.3	239	29.2	137	3.70	1.28	532	11.65	24.52	3.29
K0200	main ignimbrite	62.52	0.70	16.06	5.98	0.12	2.79	5.90	3.86	1.52	0.14	1.29	97.98	22.9	27.9	261	27.3	121	3.18	1.13	468	10.50	22.34	2.98
K0581	main ignimbrite	59.69	0.72	16.56	6.84	0.13	3.46	7.13	3.61	1.31	0.14	0.43	98.62	27.1	24.5	291	24.2	106	2.68	0.98	407	9.35	19.88	2.69
K1365	main ignimbrite	77.54	0.14	12.22	1.26	0.04	0.19	0.86	4.12	3.19	0.05	3.02	96.21	8.6	60.0	64	43.1	140	4.68	2.37	908	17.99	37.74	4.85
K1490	main ignimbrite	67.72	0.57	15.10	4.37	0.10	1.59	3.91	4.08	2.03	0.13	1.61	97.65	17.3	35.3	212	31.2	134	3.90	1.41	576	12.34	25.94	3.41
K2582a	main ignimbrite	66.09	0.59	15.44	4.71	0.11	2.03	4.60	3.91	1.94	0.19	1.60	97.99	17.3	38.8	227	28.7	150	3.88	1.63	586	12.15	25.25	3.27
K1271b	layer C bottom	61.90	0.68	16.47	6.11	0.12	2.92	6.24	3.55	1.49	0.13	1.49	98.00	23.7	27.8	279	26.0	113	2.87	1.11	451	10.20	21.51	2.83
K1270a	layer C top	65.81	0.64	15.45	5.08	0.11	1.91	4.57	4.09	1.78	0.14	2.09	97.32	18.4	30.8	235	30.1	137	3.78	1.22	515	11.47	24.30	3.18
K1269c	layer D bottom	66.54	0.59	15.40	4.69	0.10	1.84	4.46	3.96	1.90	0.12	2.26	97.00	17.8	34.2	223	30.7	133	3.71	1.38	552	12.10	25.62	3.40
K1268b	layer D top	59.92	0.72	16.55	6.84	0.13	3.45	7.11	3.42	1.30	0.14	1.26	98.07	28.4	23.8	299	24.7	100	2.55	0.96	397	9.16	19.46	2.60
K1268f	layer D top	62.04	0.70	16.13	6.37	0.12	3.00	6.17	3.41	1.52	0.14	2.11	96.97	23.4	28.6	260	26.3	114	2.99	1.13	456	10.31	21.78	2.87
K1267b	layer F bottom	65.43	0.64	15.74	5.09	0.11	1.96	4.71	4.02	1.74	0.14	1.85	97.42	22.9	28.4	262	26.9	120	3.04	1.11	467	10.38	21.90	2.90
K1267c	layer F bottom	62.95	0.67	16.04	5.91	0.12	2.74	5.84	3.63	1.56	0.13	1.63	97.46	28.4	23.8	299	24.7	100	2.55	0.96	397	9.16	19.46	2.60
K1266c	layer G top	65.13	0.64	15.78	5.10	0.11	1.99	4.86	4.15	1.70	0.14	0.39	99.10	18.5	29.8	236	29.3	134	3.37	1.19	508	11.20	23.65	3.14
K1266f	layer G top	63.42	0.65	15.75	5.76	0.11	2.69	5.71	3.71	1.69	0.13	0.38	98.63	22.0	30.9	248	26.9	120	3.06	1.24	490	10.64	22.34	2.94
K0543	S bed scoria fall	50.41	0.69	14.03	10.13	0.17	11.43	10.12	2.02	0.50	0.09	0.20	99.37	45.1	8.0	270	14.2	42	1.08	0.30	155	4.22	9.26	1.34
K1595c	S bed scoria fall	61.44	0.70	16.70	6.11	0.12	2.99	6.40	3.52	1.44	0.18	1.19	98.39	24.5	25.2	273	24.3	104	2.55	1.00	416	9.45	19.95	2.63
K2015c	S bed scoria fall	65.60	0.64	15.64	4.97	0.11	1.93	4.54	4.26	1.75	0.16	1.10	98.07	18.5	30.6	231	29.3	135	3.83	1.24	509	11.36	23.77	3.15
K0184	layer F-G	59.47	0.72	16.77	6.81	0.12	3.56	7.03	3.63	1.35	0.15	n.d.	99.70	24.4	26.1	266	24.1	106	2.77	1.07	429	9.81	20.68	2.78
K0016	Novarupta dome	76.86	0.17	12.53	1.43	0.05	0.02	0.95	4.35	3.21	0.02	n.d.	97.68	7.2	60.9	65	42.7	139	4.81	2.44	907	18.01	37.39	4.81
AM23	Naknek formation	66.20	0.52	15.80	5.57	0.08	2.61	4.48	2.41	1.62	0.09	n.d.	99.38	14.6	34.3	348	14.5	21	3.72	1.17	779	8.89	18.10	2.37

Sample #	Nd	Sm	Eu	Gd	Tb	Dy	Ho	Er	Tm	Yb	Lu	Hf	Ta	Pb	Th	U	^{226}Ra (fg/g)	$^{87}Sr/^{86}Sr$	$(^{234}U/^{238}U)$	$(^{238}U/^{232}Th)$	$(^{230}Th/^{232}Th)$	$(^{230}Th/^{238}U)$	$(^{226}Ra/^{230}Th)$
K1000a	19.59	5.30	0.79	5.66	1.02	6.53	1.42	4.05	0.64	4.06	0.66	4.59	0.83	11.51	4.762	2.327	819.9	0.70370	0.997	1.482	1.460	0.985	1.053
K1079a	19.59	5.46	0.80	5.77	1.04	6.67	1.45	4.12	0.65	4.12	0.67	4.62	0.60	11.49	4.867	2.373	799.6	n.d.	0.999	1.479	1.463	0.989	1.003
K2466b	12.63	3.66	1.04	3.90	0.69	4.37	0.94	2.58	0.40	2.43	0.40	3.11	2.26	5.74	1.130	0.516	366.3	0.70358	1.004	1.386	1.389	1.002	2.085
K2488d	13.18	3.76	1.03	4.08	0.72	4.55	0.97	2.67	0.42	2.57	0.42	3.37	1.10	5.83	3.056	1.404	574.3	n.d.	1.006	1.394	1.382	0.991	1.215
K0100c	13.12	3.75	1.03	4.05	0.72	4.63	1.00	2.84	0.43	2.77	0.45	3.55	0.42	5.76	2.817	1.333	494.3	n.d.	1.002	1.436	1.402	0.977	1.012
K0121	18.22	5.02	0.71	5.21	0.94	6.16	1.35	3.83	0.60	3.86	0.62	4.35	0.51	9.77	5.214	2.504	841.1	n.d.	0.998	1.457	1.437	0.986	0.998
K0135d	11.54	3.30	0.94	3.56	0.62	4.01	0.86	2.39	0.36	2.30	0.37	3.01	0.68	5.60	1.232	0.562	445.6	0.70368	1.002	1.385	1.381	0.997	2.339
K0162	15.17	4.27	1.14	4.60	0.81	5.25	1.10	3.12	0.48	3.03	0.50	4.17	0.50	7.02	3.303	1.567	515.6	n.d.	1.006	1.439	1.399	0.972	0.992
K0182	14.93	4.22	1.14	4.48	0.78	5.11	1.11	3.12	0.48	3.09	0.51	4.03	0.27	13.10	2.863	1.359	505.2	n.d.	1.005	1.440	1.422	0.987	1.069
K0200	13.69	3.93	1.07	4.30	0.74	4.83	1.03	2.85	0.43	2.78	0.45	3.61	0.24	7.14	2.779	1.288	466.7	0.70373	1.005	1.407	1.389	0.987	1.070
K0581	12.36	3.64	1.04	3.84	0.67	4.20	0.91	2.51	0.38	2.40	0.39	3.17	0.20	7.39	2.626	1.188	459.5	0.70368	1.003	1.372	1.369	0.998	1.119
K1365	21.19	5.80	0.86	6.09	1.11	7.11	1.56	4.39	0.69	4.35	0.70	4.84	0.41	11.63	5.215	2.494	815.2	n.d.	1.004	1.451	1.433	0.988	0.970
K1490	15.44	4.38	1.08	4.74	0.83	5.37	1.13	3.20	0.50	3.14	0.51	4.02	0.58	7.59	3.518	1.681	555.7	n.d.	0.994	1.450	1.409	0.972	0.997
K2582a	14.48	4.03	0.99	4.30	0.75	4.78	1.04	2.97	0.45	2.91	0.48	4.34	0.77	8.30	3.846	1.773	605.7	0.70362	1.001	1.399	1.402	1.002	0.999
K1271b	12.96	3.71	1.04	3.99	0.70	4.46	0.96	2.68	0.42	2.56	0.41	3.28	0.39	5.80	3.046	1.416	648.3	0.70364	1.003	1.410	1.390	0.986	1.368
K1270a	14.78	4.33	1.11	4.57	0.81	5.07	1.10	3.15	0.47	3.00	0.50	3.98	0.46	6.39	3.030	1.447	478.5	n.d.	1.002	1.449	1.402	0.968	1.006
K1269c	15.32	4.39	1.12	4.67	0.84	5.27	1.13	3.21	0.48	3.08	0.50	3.98	0.52	7.07	3.272	1.556	520.1	0.70361	1.003	1.444	1.407	0.974	1.009
K1268b	12.10	3.50	1.03	3.81	0.67	4.29	0.91	2.48	0.39	2.40	0.39	2.93	0.41	4.97	1.104	0.508	434.8	0.70370	1.003	1.395	1.395	1.000	2.522

Table 1. (continued)

Sample #	Nd	Sm	Eu	Gd	Tb	Dy	Ho	Er	Tm	Yb	Lu	Hf	Ta	Pb	Th	U	^{226}Ra (fg/g)	^{87}Sr/^{86}Sr	(^{234}U/^{238}U)	(^{238}U/^{232}Th)	(^{230}Th/^{232}Th)	(^{230}Th/^{238}U)	(^{226}Ra/^{230}Th)
K1268f	13.07	3.81	0.98	4.01	0.73	4.57	0.97	2.68	0.42	2.58	0.42	3.36	0.64	5.96	3.021	1.392	657.9	0.70373	1.001	1.398	1.390	0.994	1.399
K1267b	13.26	3.79	1.04	4.19	0.73	4.65	0.99	2.85	0.43	2.67	0.44	3.57	0.46	5.92	2.998	1.418	482.2	0.70360	1.002	1.435	1.407	0.980	1.038
K1267c	12.10	3.50	1.03	3.81	0.67	4.29	0.91	2.48	0.39	2.40	0.39	2.93	0.41	4.97	2.987	1.389	602.4	0.70374	1.005	1.411	1.399	0.991	1.288
K1266c	14.16	4.08	1.06	4.51	0.78	5.01	1.08	3.11	0.47	2.97	0.47	3.92	0.61	6.49	2.948	1.411	472.3	n.d.	1.003	1.453	1.407	0.968	1.018
K1266f	13.12	3.77	0.97	4.06	0.72	4.62	1.00	2.71	0.43	2.70	0.43	3.58	0.52	6.15	3.332	1.535	540.9	n.d.	1.003	1.398	1.389	0.993	1.044
K0543	6.53	2.13	0.67	2.40	0.41	2.59	0.55	1.51	0.22	1.37	0.22	1.36	0.07	2.39	1.030	0.435	185.6	0.70339	1.003	1.281	1.350	1.054	1.206
K1595c	12.21	3.52	0.99	3.83	0.67	4.23	0.90	2.48	0.39	2.40	0.39	3.09	0.19	5.81	2.888	1.330	522.2	0.70371	1.002	1.397	1.389	0.994	1.163
K2015c	14.23	4.12	1.05	4.41	0.78	5.02	1.07	3.07	0.46	3.00	0.49	3.98	0.86	6.28	3.017	1.438	473.0	n.d.	1.003	1.446	1.408	0.974	1.004
K0184	12.65	3.61	0.99	3.89	0.68	4.27	0.93	2.60	0.39	2.43	0.40	3.21	0.21	5.10	1.475	0.674	398.1	0.70374	1.005	1.387	1.384	0.998	1.741
K0016	20.81	5.68	0.84	5.90	1.07	7.15	1.53	4.41	0.69	4.46	0.72	5.05	0.41	11.99	5.312	2.525	870.2	0.70372	1.002	1.442	1.428	0.990	1.042
AM23	9.57	2.22	0.90	2.33	0.38	2.29	0.49	1.43	n.d.	1.42	0.22	0.87	0.47	6.41	2.460	0.960	n.d.	0.70480	n.d.	1.184	n.d.	n.d.	n.d.

[a]In Inferred Stratigraphic Order from bottom to top of the sequence; major elements are in wt % and trace elements are in ppm unless otherwise specified; n.d., not determined.

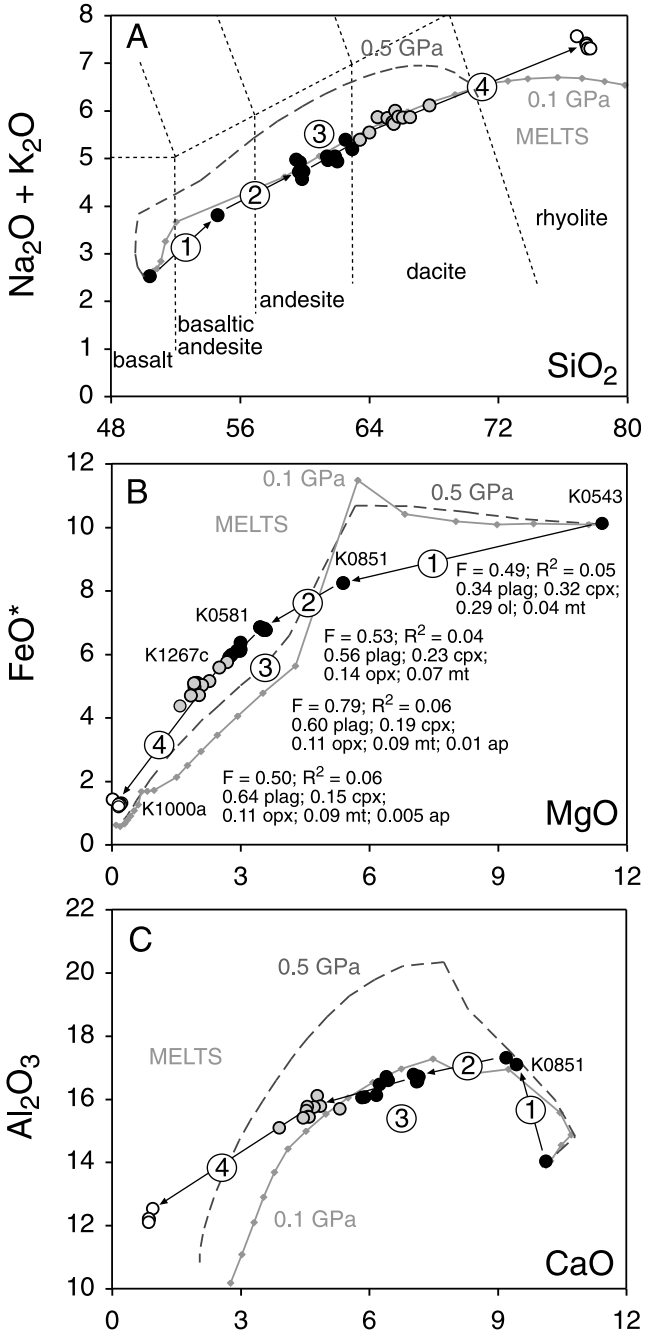

Figure 4. Plots of (a) total alkalis versus SiO_2, (b) FeO* versus MgO, and (c) Al_2O_3 versus CaO showing the compositional range of the products of the 1912 eruption (solid, shaded, and open circles designating the basalt-andesite, dacite, and rhyolite compositional ranges, respectively, are used in this and subsequent figures). Note that the curvature of the trends precludes models involving pure two-end-member mixing. Also shown are the results of a four-stage least squares model of fractional crystallization (see Table 2) and the results of MELTS modeling at 0.1 GPa (shaded line) and 0.5 GPa (dashed shaded line).

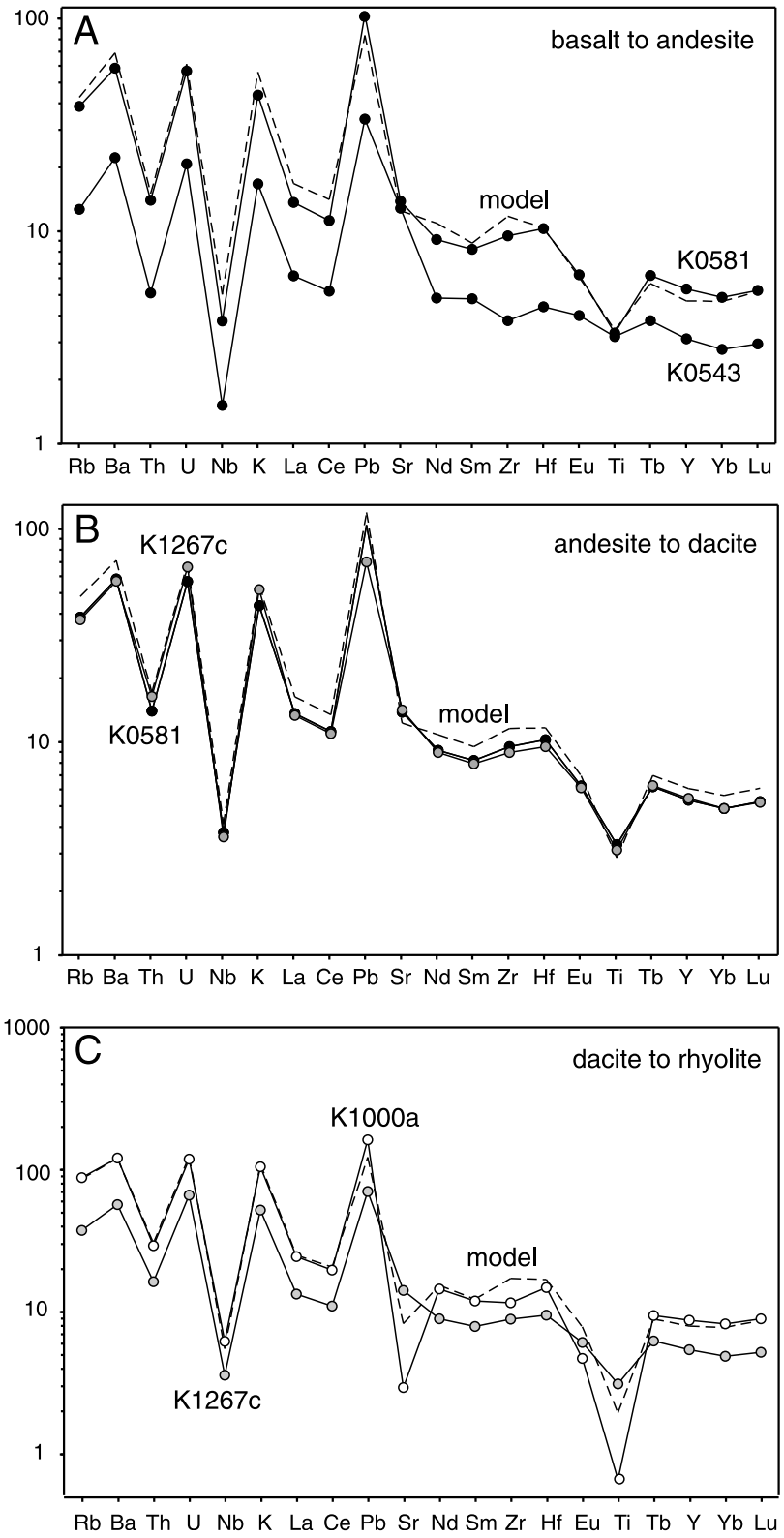

Figure 5. Primitive-mantle normalized incompatible trace element diagrams showing the general parallelism of patterns for the basalt (K0543), andesite (K2466b), and rhyolite (K1000a) used in fractional crystallization modeling; the results are shown as dashed lines.

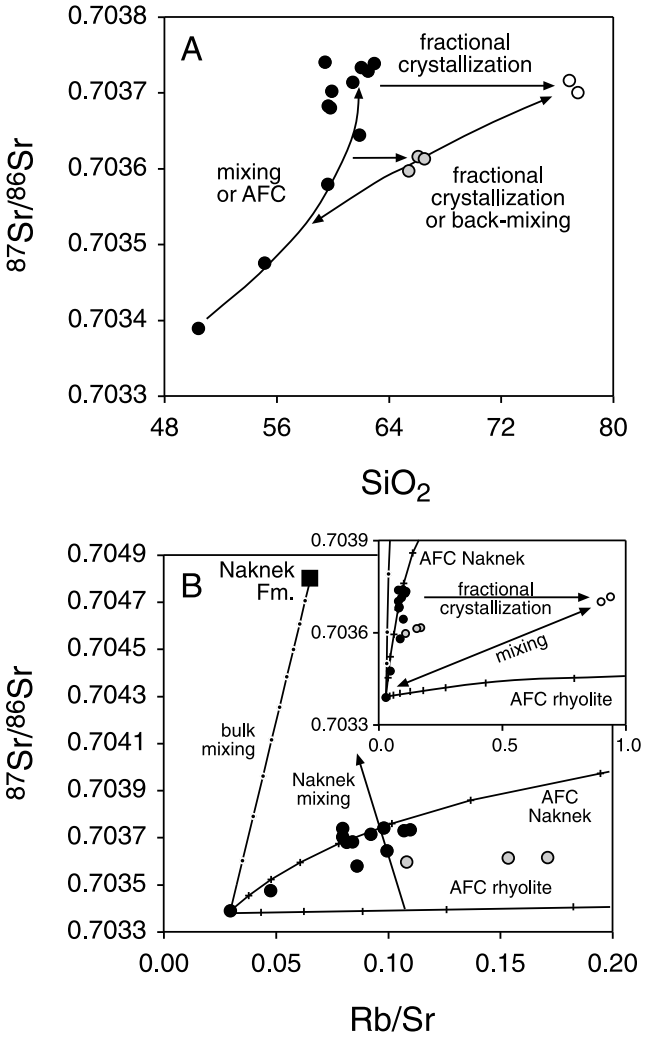

Figure 6. (a) Plot of $^{87}Sr/^{86}Sr$ versus SiO_2 with hypothetical liquid evolution trends discussed in the text. (b) Plot of $^{87}Sr/^{86}Sr$ versus Rb/Sr showing model trends for mixing (in 10% increments) between the basalt and the Naknek Formation sediment from Table 1 and also fractional crystallization combined with assimilation (AFC) of both the Naknek sediment and silicic material assumed to have the composition of rhyolite K1000a (ticks indicate increments of 10% crystallization; *r*, the rate of crystallization to assimilation, was set at 0.3). Inset shows an expanded scale to include the rhyolites. The bulk partition coefficients (D_{Sr} = 1.021, D_{Rb} = 0.046) were calculated from the data in Table 3 assuming a fractionating assemblage composed of 60% plagioclase, 30% pyroxene, 9% magnetite, and 1% apatite.

concentrations and an $^{87}Sr/^{86}Sr$ ratio of 0.70480. We accept that this is a single sample; the Naknek Formation overall is likely to be significantly more isotopically diverse.

[19] Glassy pumice clasts are susceptible to surficial alteration that can lead to loss of ^{234}U situated in recoil-damaged sites. However, all but one of the samples analyzed has ($^{234}U/^{238}U$) within 2σ analytical error (6 ‰) of 1 (Table 1). As shown in Table 1, Th content increases from 1.03 to 5.32 ppm and U from 0.43 to 2.53 ppm between the basalt and the rhyolites. Over the same compositional spectrum, ($^{238}U/^{232}Th$) ranges from 1.28 to 1.48 and ($^{230}Th/^{232}Th$) from 1.35 to 1.46, leading to a restricted range in ($^{230}Th/^{238}U$) from 0.97 to 1.05, overlapping the range observed from the Alaska-Aleutian arc in general [*George et al.*, 2003]. The new U-Th isotope data are also in excellent agreement with earlier Katmai data reported by *Reagan et al.* [2003]. On a U-Th equiline diagram (Figure 7a), the basalt and basaltic andesites lie to the left of the equiline with 5–7% ^{230}Th excess. While this is unusual in oceanic arcs, it is relatively common in arcs developed on thicker crust such as the Alaskan Peninsula [e.g., *George et al.*, 2003]. In all other respects, these more mafic rocks have the typical arc signature characterized by other Katmai rocks. In contrast, the andesites and dacites have up to 3% ^{238}U excesses and form an array extending from and to the right of the equiline. Excepting the Novarupta Dome sample and the rhyolites, the bulk of the samples in the basalt to dacite compositional range scatter about the 40 kyr reference line for Katmai andesites and dacites observed by *Reagan et al.* [2003]. Finally, the rhyolites have some of the

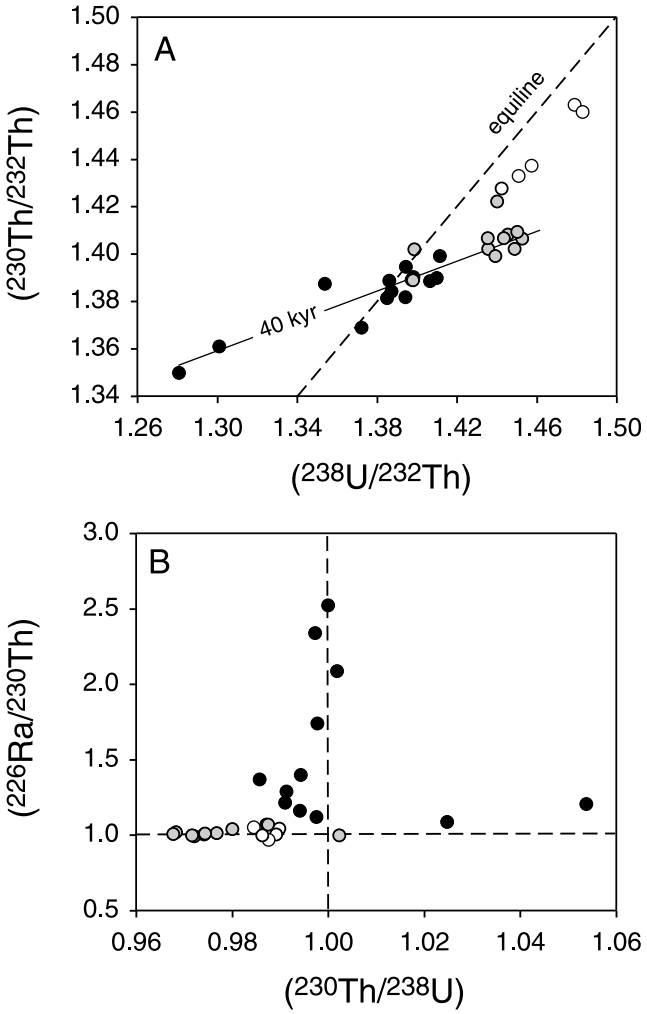

Figure 7. Plots of (a) U-Th equiline diagram and (b) ($^{226}Ra/^{230}Th$) versus ($^{230}Th/^{238}U$) with a 40 kyr isochron superimposed from *Reagan et al.* [2003]. Dashed lines represent secular equilibrium.

Table 2. Input Parameters and Results of Least Squares Models

Parent Magma	Daughter Magma	% of Total Crystallization	Mineral Fractions in Cumulate						R^2
			Olivine	Clinopyroxene	Orthopyroxene	Plagioclase	Magnetite	Apatite	
Stage 1: Basalt to Basaltic Andesite									
K0543	K0851	51	29	32	0	34	4	0	0.05
Stage 2: Basaltic Andesite to Andesite									
K0851	K0581	47	0	23	14	56	7	0	0.04
Stage 3: Andesite to Dacite									
K0581	K1267c	21	0	19	11	60	9	1	0.06
Stage 4: Dacite to Rhyolite									
K1267c	K1000a	50	0	15	11	64	9	0.5	0.06
Mineral Compositions (Stages 1 and 2)[a]									
SiO_2			38.35	53.00	53.00	52.90	0.00	0.00	
TiO_2			0.00	0.37	0.25	0.00	8.60	0.00	
Al_2O_3			0.03	2.30	1.46	29.90	3.41	0.00	
FeO total			21.16	7.95	18.10	0.00	78.90	0.21	
MgO			40.24	16.55	25.40	0.00	3.02	0.54	
CaO			0.16	20.00	1.33	12.67	0.00	52.40	
Na_2O			0.00	0.18	0.03	4.15	0.00	0.00	
K_2O			0.00	0.00	0.00	0.00	0.00	0.00	
P_2O_5			0.00	0.00	0.00	0.00	0.00	40.98	
Mineral Compositions (Stage 3)[b]									
SiO_2				51.00	52.70	54.00	0.00	0.00	
TiO_2				0.55	0.23	0.00	9.50	0.00	
Al_2O_3				2.40	2.60	29.70	2.45	0.00	
FeO total				9.10	16.40	0.00	79.90	0.21	
MgO				14.80	25.80	0.00	2.20	0.54	
CaO				20.90	1.59	11.50	0.00	52.40	
Na_2O				0.30	0.01	4.90	0.00	0.00	
K_2O				0.00	0.00	0.19	0.00	0.00	
P_2O_5				0.00	0.00	0.00	0.00	40.98	

[a]Core compositions from K140 andesite [*Hildreth*, 1983, and unpublished data].
[b]Core compositions from K101 dacite [*Hildreth*, 1983, and unpublished data].

highest U/Th ratios in the sample suite and are displaced to higher ($^{230}Th/^{232}Th$) ratios below the equiline and above the dacites.

[20] The first Ra data from Katmai are presented in Table 1. ^{226}Ra concentrations range from 185 to 870 fg/g and ($^{226}Ra/^{230}Th$) ratios from 0.97 to 2.52. The lowest values are from the rhyolites and highest silica dacites, and it is likely that these samples are in secular equilibrium. Given the likely accuracy of the measurements (limited by the 3% uncertainty on the NIST 4969 ^{226}Ra standard), we consider the intrinsic range of ($^{226}Ra/^{230}Th$) to be from 2.52 to 1. On a plot of ($^{226}Ra/^{230}Th$) versus U-Th disequilibria (Figure 7b), the basalt and basaltic andesites, which both have ($^{230}Th/^{238}U$) > 1, have moderate ($^{226}Ra/^{230}Th$) values of 1.21–1.09. Andesites, which are characterized by near equilibrium ($^{230}Th/^{238}U$), have a wide range of ($^{226}Ra/^{230}Th$) values (1.07–2.52). This range is similar to that (1–2.2) reported for all Aleutian and Alaskan arc front volcanoes [*George et al.*, 2003, 2004]. With three exceptions, essentially all of the Katmai dacites and rhyolites are within 2σ analytical error (1%) of Ra-Th secular equilibrium. The exceptions are three dacites (K1276b, K0182, and K0016) with 4–7% ^{226}Ra excesses. Combined, the ^{238}U–^{230}Th–^{226}Ra data imply that the andesite-dacite array is not a 40 kyr isochron representing an instantaneous fractionation event, but an array that must have been generated by a process or processes operating over a variety of timescales.

5. Geochemical Modeling

[21] The products found in the Valley of Ten Thousand Smokes come from one of the most studied eruptions on Earth, so it is surprising that these products have received little quantitative geochemical treatment. Given the historical development of ideas, we begin by assessing the extent to which the simplest closed-system model can account for the data and then show how both long- and short-lived isotopes and numerical thermal models require an open-system.

5.1. Major Elements

[22] The major element, trace element, and Sr isotope trends are consistent with the variation being *dominated* by fractional crystallization, and we chose in the first instance to model this using a simple least squares numerical approach. The results, including phase compositions and proportions, are documented in Table 2 and illustrated in Figure 4, showing that it is possible to broadly simulate the suite in four successive stages of crystallization from basalt (K0543) to basaltic andesite (K0851) to andesite (K0581) to dacite (K1267c) and finally to rhyolite (K1000a). The minimization used mineral compositions obtained from the andesites

and dacites themselves [*Hildreth*, 1983, also unpublished data, 2009]. The fractionating assemblage is essentially gabbroic and involves apatite in the final two steps, consistent with a rapid decrease in P_2O_5 between the dacites and the rhyolites (not shown). The calculated mineral proportions differ somewhat from the modal assemblages in the rocks, but the latter can be partly entrained during magma migration [*Price et al.*, 2005] and are clearly not the crystals that separated from the liquids to produce the bulk compositional range. The calculations yielded very satisfactory fits (sums of residuals squared <0.1), bearing in mind the very large compositional range being simulated (see Table 2).

[23] To calibrate the temperatures of the system at differing degrees of fractionation for eventual use in constraining the potential timescale of crystallizing the Katmai magma body, we next used the MELTS software algorithm [*Ghiorso and Sack*, 1995; *Asimow and Ghiorso*, 1998]. The starting composition was the composition of basalt K0543, and we used 25°C steps between the calculated liquidus (1279°C) until rhyolitic compositions were achieved near the solidus at 794°C. Additional input parameters were an oxygen fugacity buffered at QFM +2 log units, which is consistent with the fO_2 values calculated using coexisting oxides for the Katmai ejecta (Figure 3), and a pressure of 0.1 GPa, which is in line with the experimental findings of *Coombs and Gardner* [2001] and *Hammer et al.* [2002]. The starting basalt was assigned 0.8 wt % H_2O, and this led to calculated H_2O contents of 1.5 wt % in the andesite, 2.2 wt % in the dacite, and 3.8 wt % in the rhyolite, which is closely consistent with the melt inclusion observations of *Westrich et al.* [1991] (see Figure 3). As noted by *Westrich et al.* [1991], these H_2O contents would lead to saturation of the andesites, dacites, and rhyolites at depths of 4, 2, and 0.5 km, respectively.

[24] Figure 8 shows the extent of crystallization and change in SiO_2 versus temperature drop calculated by the MELTS model. The liquidus of the K0543 was determined to be 1279°C. Half of the crystallization occurs over a 150°C temperature interval from 1144°C–994°C that corresponds to the evolution of the predicted liquid composition from basaltic andesite to dacite (51 wt %–66 wt % SiO_2). Interestingly, the rate of crystallization increase per °C is significantly lower across the range of 68 wt %–77 wt % SiO_2, so the origin of the silica gap probably reflects the physics of extraction of interstitial liquid from a crystal mush or eutectic remelting of silicic rocks.

[25] In Figure 8b, we also compare the SiO_2-temperature relationship from the MELTS model, with the oxide temperatures from *Hildreth* [1983] shown in Figure 3, as well as water-saturated liquidus temperatures for andesite, dacite, and rhyolite, experimentally constrained by *Coombs and Gardner* [2001] and *Hammer et al.* [2002]. The temperatures predicted by MELTS are somewhat higher than the range measured using groundmass oxides from the andesite. The water-saturated experimental liquidus for the andesitic composition is 55°C–35°C lower than the significantly water-undersaturated MELTS model. The comparison for the dacite is better, and the agreement of the MELTS and oxide temperatures for the rhyolite, which is nearly aphyric, is excellent. The experimental and calculated liquidus temperatures for the rhyolite and dacite compositions are nearly identical, which are water saturated and nearly water saturated, respectively, in the MELTS models. Thus, MELTS appears to do a reasonable job in simulating the energy constraints of the system, providing confidence to use the extent-of-crystallization versus temperature function in the numerical thermal models described subsequently.

[26] Although it was not our primary purpose, the calculated liquid line of descent from the MELTS model is also compared with the whole rock data in Figure 4. The simulation is generally satisfactory through the intermediate magmas, bearing in mind the extreme compositional and crystallization range being simulated. However, MELTS is known to work less well for minimum melt compositions. Thus, at very high degrees of crystallization (required to generate the rhyolites) the MELTS model overestimated the SiO_2 content and underestimated the Al_2O_3 and alkali contents of the rhyolites because of feldspar crystallization that may be unrealistically extensive. FeO* is also underestimated across the andesite-dacite compositional range because of the rapid removal of magnetite near 1100°C by the MELTS program. In light of the imperfect fit of this MELTS model to the data, we chose to use the phase proportions and extents of crystallization from the least squares modeling in the trace element modeling described in section 5.2.

[27] Although the experimental studies indicate a shallow level origin for the evolution of the Katmai eruptives, it is conceivable that these simply reflect the last pressure of equilibration (i.e., shallow-level assembly) of magmas whose bulk composition was determined at greater depth. For example, *Annen et al.* [2006] have suggested that some intermediate to silicic arc magmas are produced in lower crustal hot zones. For the Katmai products, the lack of depletion in the heavy rare earth elements (see Figure 5) clearly precludes a lower crustal origin, since garnet will be stable at these depths. Evolution at midcrustal levels is harder to assess, but MELTS modeling of crystallization performed at 0.5 GPa provided significantly poorer fits to the data (see Figure 4) than the 0.1 GPa model. This is due to the early onset of orthopyroxene crystallization and subsequent orthopyroxene-plus-clinopyroxene crystallization, which causes SiO_2 concentrations to initially decrease and then rapidly increase when magnetite begins to fractionate. Higher pressures also lead to the late onset of plagioclase crystallization, which elevates concentrations of Al_2O_3 above those observed in the Katmai samples (Figure 4c). The high modal pyroxene in the crystallizing assemblage along the entire liquid line of descent also causes greater enrichment in incompatible element abundances at a given SiO_2 concentration in the 0.5 GPa model than that observed in the Katmai samples (Figure 4a). The sharp variations in the slope of FeO* concentrations, when plotted against measures of fractionation such as MgO (Figure 4b), contrast with the consistent changes in slope observed for Katmai lavas. This contrast implies that some internal mixing in the basalt through andesite compositional range could have occurred. However, the closer fit of observed compositional trends and the model trends at 0.1 GPa, as compared to the trends at 0.5 GPa, suggests that the bulk compositions of the Katmai magmas were not formed in the deep or even middle crust but rather at shallow depths.

[28] In both the least squares and the MELTS models, the total extent of crystallization from basalt K0543 to rhyolite K1000a is 80–90%, and so for an erupted rhyolite volume of 7.2 km^3, the implied volume of parental basalt is of the order

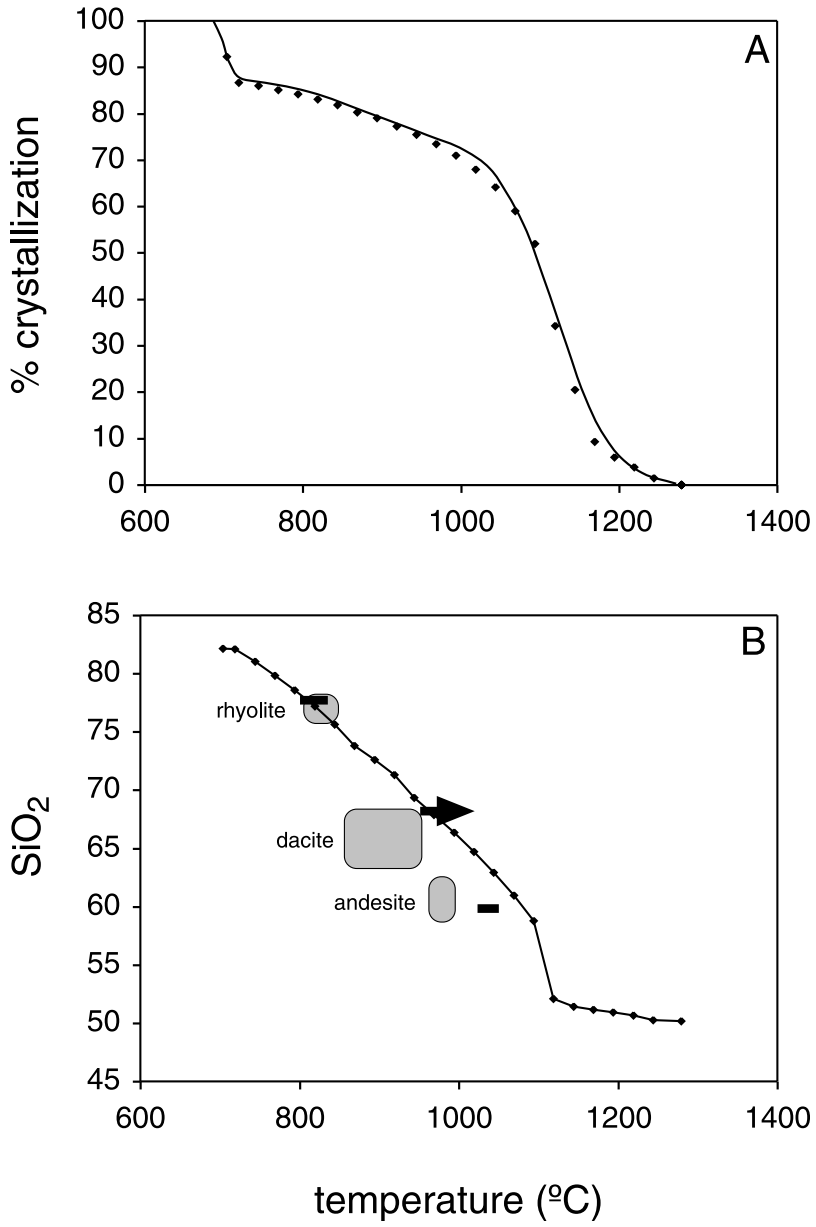

Figure 8. Plots of (a) extent of crystallization and (b) SiO_2 versus temperature for the Katmai system from the MELTS modeling. The curve on Figure 8a shows the fit of the parameterized crystallization function from section 7 to the MELTS output (black diamonds). In Figure 8b, the shaded boxes indicate the temperature ranges for andesite, dacite, and rhyolite obtained from Fe-Ti oxide thermometry [*Hildreth*, 1983]. Horizontal lines indicate the experimentally determined (H_2O-saturated) liquidus temperatures for the andesite, dacite, and rhyolite from *Hammer et al.* [2002]. For the dacite, the experimental temperature is shown as a arrow indicating the minimum appropriate temperature for this composition.

of 65 km^3. Evolution from an andesitic composition (e.g., K0581) requires only 59% crystallization and a calculated volume of 17 km^3, similar to that estimated by *Hildreth and Fierstein* [2000].

5.2. Trace Elements

[29] In order to further test the major element modeling, the phase proportions and extents of crystallization from the least squares models were combined with the published partition coefficient data listed in Table 3 in a Rayleigh fractional crystallization simulation of the incompatible trace element variation across the suite. Separate partition coefficients for the basalt-to-dacite and dacite-to-rhyolite stages were taken from *Rollinson* [1993] with the following exceptions. The clinopyroxene rare earth-element partition coefficients were calculated following the method outlined by *Wood and Blundy* [1997]. For U and Th the plagioclase partition coefficients were taken from *Blundy and Wood* [2003], while their inferred Ra partition coefficient of 0.03 lies in the range determined experimentally by *Miller et al.* [2007] and

Table 3. Partition Coefficients Used in Trace Element Modeling[a]

	Olivine	Orthopyroxene	Clinopyroxene	Plagioclase	Magnetite	Apatite
			Basalt to Andesite to Dacite			
Rb	0.03	0.02	0.05	0.04	0.15	0
Ba	0.03	0.006	0.006	0.17	0	0.13
Ra	0	0.002	0.002	0.03	0	0.1
Th	0.00031746	0.008	0.008	0.0034	0.09	1.18
U	0.002	0.0083	0.0083	0.0006	0	0.74
Nb	0.01	0.13	0.027	0.026	0.7	52.6
K	0.007	0.009	0.015	0.1	0.045	0
La	0.0002	0.0031	0.257	0.32	0.055	0
Ce	0.00007	0.0021	0.426	0.21	0.096	0.73
Pb	0.0003	0.0014	0.0075	0.7	0.019	0
Sr	0.01	0.15	0.075	2.41	0.11	0.518
Nd	0.0003	0.0023	0.939	0.14	0.25	0
Sm	0.01	0.0037	1.492	0.11	0.32	0
Zr	0.012	0.18	0.26	0.048	0.127	4.76
Hf	0.0029	0.019	0.33	0.06	4	0
Eu	0.01	0.02	1.709	0.34	0.062	0
Ti	0.015	0.205	0.265	0.083	16.5	0
Gd	0.002	0.0085	1.885	0.09	0	0
Tb	0.002	0.0085	2.003	0.09	0.52	0
Dy	0.002	0.0085	2.053	0.09	0	0
Y	0.0082	0.015	2.048	0.04	0.52	0
Yb	0.024	0.038	1.755	0.04	0.5	0
Lu	0.024	0.038	1.637	0.06	0.43	0
			Dacite to Rhyolite			
Rb		0.02	0.05	0.04	0.15	0
Ba		0.006	0.006	0.17	0	0.13
Ra		0.002	0.002	0.03	0	0.1
Th		0.008	0.008	0.0034	0.09	1.18
U		0.0083	0.0083	0.0006	0	0.74
Nb		0.13	0.027	0.026	0.7	52.6
K		0.009	0.015	0.1	0.045	0
La		0.0031	0.412	0.32	0.055	0
Ce		0.0021	0.696	0.21	0.096	0.73
Pb		0.0014	0.0075	0.7	0.019	0
Sr		0.15	0.075	2.41	0.11	0.518
Nd		0.0023	1.57	0.14	0.25	0
Sm		0.0037	2.504	0.11	0.32	0
Zr		0.2	0.6	0.135	0.8	4.76
Hf		0.019	0.33	0.06	4	0
Eu		0.02	2.859	0.34	0.062	0
Ti		0.205	0.265	0.083	16.5	0
Gd		0.0085	3.133	0.09	0	0
Tb		0.0085	3.299	0.09	0.52	0
Dy		0.0085	3.341	0.09	0	0
Y		0.015	3.304	0.04	0.52	0
Yb		0.038	2.699	0.04	0.5	0
Lu		0.038	2.484	0.06	0.43	0

[a]On the basis of *Wood and Blundy* [1997], *Blundy and Wood* [2003], *Prowatke and Klemme* [2006], and the compilation by *Rollinson* [1993]. Ba, Ra, Th and U values for pyroxene are based on measured bulk pyroxene data from *Reagan et al.* [2003], adjusted for glass contamination, and guided by *Blundy and Wood* [2003].

Fabbrizio et al. [2009]. Bulk pyroxene U and Th partition coefficients were derived from measured bulk pyroxene data from Katmai andesite and dacite [*Reagan et al.*, 2003] which were adjusted for glass contamination and guided by the lattice-strain model of *Blundy and Wood* [2003]. The apatite partition coefficients represent the averages of samples 77 and 61B analyzed by *Prowatke and Klemme* [2006].

[30] The results of the trace element modeling are compared with the observed trace element compositions of samples K0581, K1267c, and K1000a in Figure 8. Although some elements were better modeled than others, the general shape of the patterns was reasonably well approximated in each stage. This provides validation that the overall extents of fractionation and the resultant volume calculations determined from the major element treatment are reasonably robust. In detail, there are discrepancies present for some elements like Ti, Zr, and P which probably reflect some combination of errors resulting from the partition coefficients chosen and the phase proportions from the least squares modeling. For example, inflections in both Zr and P_2O_5 concentrations around 65 wt % SiO_2 (not shown in Figure 8) suggest the onset of accessory phase crystallization in the magmas. Apatite is commonly found in thin section, whereas zircon is generally not. Nevertheless, the zircon saturation calculations [*Watson and Harrison*, 1983] indicate that the rhyolites would crystallize zircon at a temperature <900°C that is significantly hotter than that inferred for these rocks in the experiments of *Coombs and Gardner* [2001] and in the MELTS model presented above. Thus, zircon should have

crystallized over an interval of up to 100°C, and we note that *Lowenstern* [1993] has observed tiny zircon crystals adhering to quartz phenocrysts in the rhyolite. Irrespective of these caveats, the trace element modeling concurs with the major element results since both show that closed-system fractionation can explain much of the variation in Katmai magma compositions.

5.3. Sr Isotopes

[31] Despite the observation that a simple fractional crystallization model does a good job at explaining the first-order variation in the compositional data, the new Sr isotope results preclude production of the different Katmai rocks via closed-system differentiation of a common parental magma. Moreover, as the hypothetical evolutionary paths sketched on Figure 6a illustrate, there is no single liquid line of descent that can link all of the products. Some form of mixing or coupled assimilation and crystal fractionation (AFC) is required by the basalt-andesite array. The rhyolites could then be produced by fractional crystallization from the most radiogenic andesites, whereas the dacites could be produced either by fractional crystallization, from magmas with Sr isotope compositions like the less radiogenic basaltic andesite parents, or by back-mixing between the rhyolites and the basaltic andesites (see Figure 6a). An alternative scenario is one in which the system is built up over time by multiple injections of magmas [e.g., *Jellinek and DePaolo*, 2003; *Annen et al.*, 2008] with variable $^{87}Sr/^{86}Sr$ compositions.

[32] Potential assimilants include the Naknek Formation sediments, within which the Katmai magmas are inferred to have been stored [*Hildreth and Fierstein*, 2000], and older silicic material. In a model of progressive magma chamber build-up [e.g., *Annen et al.*, 2008], this could represent recently solidified fractionated magma that evolved from earlier injections of mafic magma. Such material would accordingly be anticipated to be similar in composition to the erupted rhyolites [*Reagan et al.*, 2003]. Evidence for the involvement of solidified silicic rocks is provided by the presence of granitic clasts in the final ejecta around Novarupta dome [*Hildreth and Fierstein*, 2000].

[33] Two-end-member mixing will be linear on the $^{87}Sr/^{86}Sr$ versus Rb/Sr plot on Figure 6b, and a mixing vector between the basalt and a Naknek sediment composition completely misses the Katmai data array. The inset to Figure 6b shows that simple mixing between the primitive basalt and the rhyolites cannot account for the composition of the dacites, nor can back-mixing between the rhyolites and andesites (banded pumice fragments indicate that magma mingling, rather than magma mixing, occurred [*Hildreth and Fierstein*, 2000]. In any case, the curvilinear trends observed for several major and trace elements (compare with Figures 4b and 4c) preclude simple two-end-member mixing models that may be important in other arc volcanic systems [e.g., *Price et al.*, 2005; *Reubi and Blundy*, 2009].

[34] One potential explanation for the variation in the Sr isotopic compositions in Katmai lavas is assimilation during fractional crystallization (AFC). In Figure 6b we show the results of AFC modeling [*DePaolo*, 1981] using both the Naknek sediments (AM23 from Table 1) and a rhyolite as potential contaminants (we chose sample K1000a for this purpose). Bulk partition coefficients (D_{Sr} = 1.021; D_{Rb} = 0.046) were based on the trace element modeling described previously (see Table 3). As can be seen, assimilation of the Naknek sediments during fractional crystallization can account for increasing $^{87}Sr/^{86}Sr$ among the basalt-andesite array. The rate of assimilation to fractional crystallization (r) was chosen to be 0.3, as inferred to be typical of many magmatic systems. Note that because the Naknek sediment has a broadly similar composition to the dacites (see Table 1), moderate amounts of assimilation will not significantly affect the major element composition of the Katmai magmas. Replication of the $^{87}Sr/^{86}Sr$ ratios of the rhyolites and some of the dacites requires an additional and subsequent period of closed-system fractional crystallization. Alternatives to account for the composition of the andesites and dacites include AFC involving silicic material followed by contamination by the Naknek sediments (see Figure 6b) or injections of magma with varying $^{87}Sr/^{86}Sr$. Narrowing the possibilities between these sequences of events is possible using the U-series data.

6. U-Series Constraints and the Time Scales of Magmatic Evolution

[35] It is generally accepted that U-series disequilibria in young volcanic rocks are inherited from the mantle, and convergent margin volcanic rocks typically preserve U-Th-Ra disequilibria produced by fluid addition to their source regions [*Turner et al.*, 2003]. The U-series data presented here span a significant compositional range for an individual eruption and support the Sr isotope evidence for open-system magmatic evolution beneath Katmai. As noted in many previous studies, closed-system fractionation in the absence of significant modal proportions of accessory phases has a limited ability to fractionate U/Th ratios because both elements are highly incompatible. This is well illustrated by the calculated 90% fractionation vector in Figure 9a. An inescapable consequence is that internally differentiated products from closed systems are predicted to show little or no variation in U-Th isotopes, and this is clearly not the case at Katmai. The data therefore requires either input of magmas with variable U/Th ratios, assimilation of a material with high U/Th, or fractionation of accessory phases with $D_{Th} > D_U$.

[36] We explore this by transposing the same mixing and AFC models discussed previously onto the U-Th equiline and ($^{226}Ra/^{230}Th$) versus Th concentration diagrams shown in Figure 9. As for Figure 6b, two-end-member mixing is linear on the U-Th equiline diagram. However, mixing with the Naknek sediment or silicic plutonics is precluded by the Sr isotope-Rb/Sr relationships shown in Figure 6b. The two models of AFC, followed by subsequent bulk mixing with the Naknek sediment that could satisfactorily explain the Sr isotope data on Figure 6b, are also plotted in Figure 9. It is clear from Figure 9a, assuming the basalt as a starting composition, that AFC involving the Naknek sediment cannot account for the data, leading instead to a negative sloped trend.

[37] AFC involving silicic material does a better job at simulating the data, producing a positive trend that encompasses much of the U-Th range of the basalt-andesite array (see Figure 9a). However, it does not reach the compositions of the dacites or rhyolites and extrapolation of this AFC curve would pass above the data at significantly higher ($^{230}Th/^{232}Th$). The reason for this is that the low partition

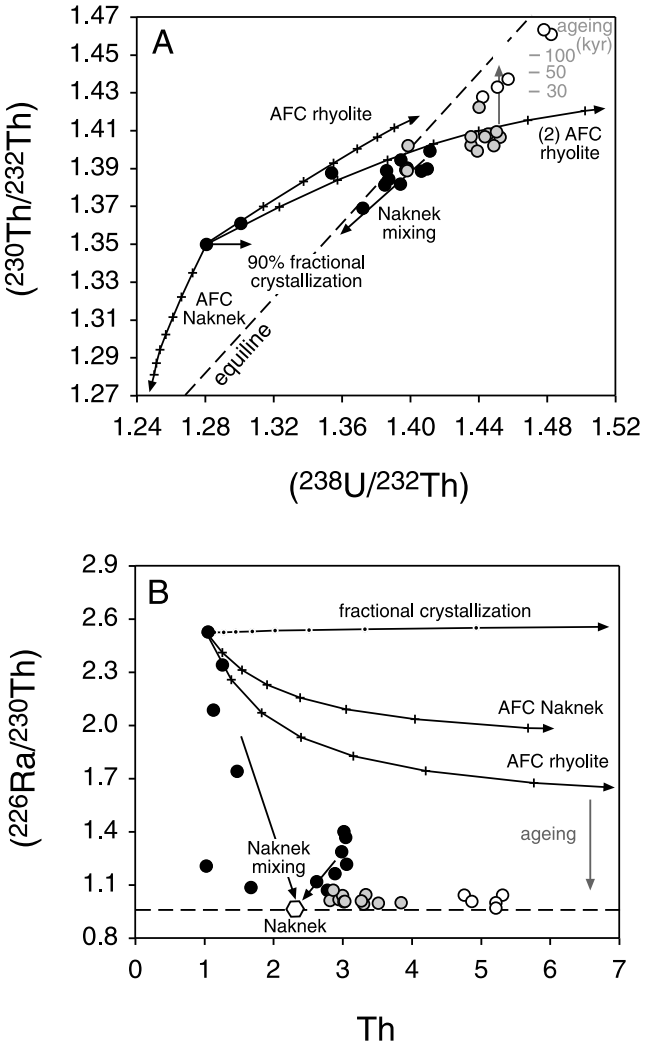

Figure 9. Plots of (a) U-Th equiline diagram and (b) (^{226}Ra/^{230}Th) versus Th showing the results of numerical fractionation and combined assimilation and fractionation (AFC) models (in 10% increments) using the same input parameters as those detailed for Figure 6b (D_U = 0.0193, D_{Th} = 0.0243, D_{Ra} = 0.02). The U-series composition of the Naknek sediment was calculated from its measured U and Th concentrations and assuming secular equilibrium. The model labeled "(2) AFC rhyolite," in Figure 9a assumed bulk Th and U partition coefficients of 0.265 and 0.205, respectively. The effects of additional aging from the latter model curve to simulate the (^{230}Th/^{232}Th) ratios of the highest U/Th rhyolites are indicated on the equiline diagram.

coefficients for U (and Th) do not allow the full U/Th range of the data to be reproduced. An additional AFC model using higher partition coefficients, as shown in Figure 9a, can provide a better approximation to the full basalt-dacite compositional array (we return to the rhyolites later). Subsequent mixing with the Naknek sediment (compare with Figure 6b) could explain the displacement of some of the samples below this model curve to lower (^{230}Th/^{232}Th). However, partition data for phases in intermediate to silicic magmas remain much less well constrained than in more mafic systems. The higher partition coefficients used in this model lie at the upper end of those typically measured as well as the ranges reported in compilations such as those by *Rollinson* [1993]; they would likely require fractionation of an accessory phase with $D_{Th} > D_U$ such as apatite, but not zircon. Whereas this scenario cannot be ruled out, if the variation in U/Th is related to assimilation of a high U/Th material and fractional crystallization, then U-Th should vary with measures of differentiation such as SiO_2. While this appears to be broadly true of the 1912 ejecta, it is not true when one considers the compositions of lavas erupted from the geographically larger magmatic system. For example, an andesite lava erupted from Trident in 1959 has a U-Th composition that is more similar to the Katmai dacites, whereas the Falling Mountain and Cerberus dacite domes have compositions more akin to the Katmai andesites [see *Reagan et al.*, 2003].

[38] A more probable explanation for the variation in U/Th and Sr isotope *ratios* in the Katmai magmas is that the basaltic magmas feeding the system varied in composition with time (Figure 10a). In this scenario, variations in the major and trace element concentrations would remain dominated by fractional crystallization. However, U/Th and Sr

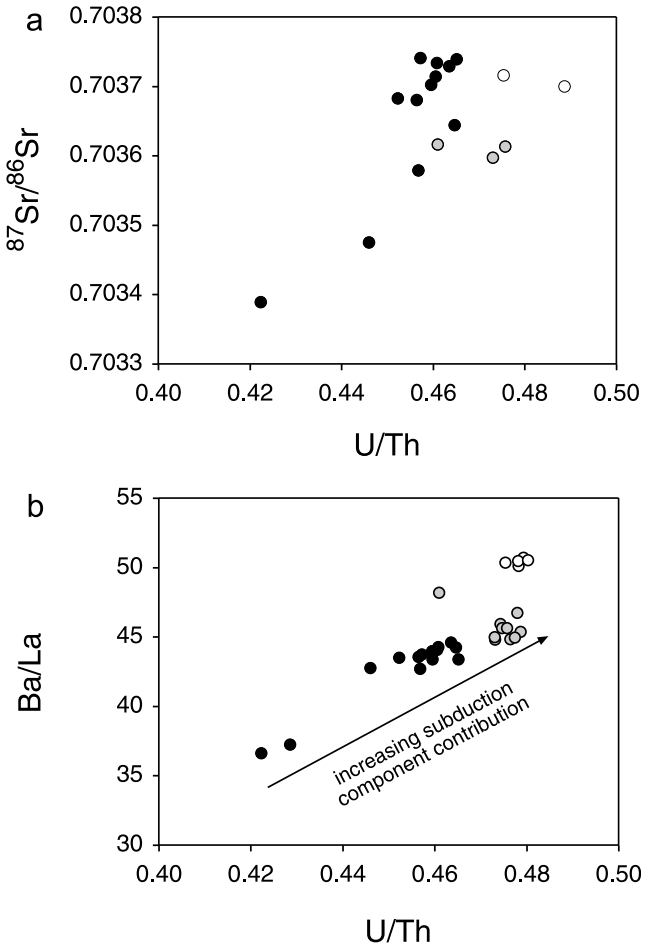

Figure 10. Plots of (a) ^{87}Sr/^{86}Sr and (b) Ba/La versus U/Th showing the good correlation for the Katmai rocks that suggest variable slab-derived signatures in the contributing magmas.

isotope ratios changed because these ratios were higher for the earlier mafic magmas that differentiated to form the Katmai andesites, dacites, and rhyolites compared with those magmas more recently intruded into the system as represented by the erupted basalt and basaltic andesites. U-Th data for mafic lavas from the continental portion of the Aleutian arc show such variability [*George et al.*, 2003]. Additional support for this contention can be found in the observation that only the basalt and basaltic andesite with ^{230}Th-excesses have $^{87}Sr/^{86}Sr$ values less than 0.7035, whereas all other samples have ($^{230}Th/^{238}U$) $\leq$ 1 and $^{87}Sr/^{86}Sr$ values in the range of 0.7036–0.7037. This can be attributed to the latter samples having a slightly elevated contribution of Sr from the subducting slab compared with the former (Figure 6a and Table 1). The good correlation of U/Th with Ba/La (Figure 10b) for Katmai ejecta also suggests that the magmas feeding this system had varying contributions from subducted components. These changes would need to have occurred on a timescale less than the lifetime of U-Th disequilibria (~350 kyr) and they are thus unlikely to reflect changes in the thermal state of the subducting plate. However, they could reflect changes in subducted fluid contributions [*Turner et al.*, 2003], or perhaps the assemblage of residual accessory phases in the slab that can control the contributions of Th and La relative to more fluid mobile elements like U, Sr, and Ba [e.g., *Kessel et al.*, 2005; *Klimm et al.*, 2008; *Plank et al.*, 2009].

[39] Our new ^{226}Ra disequilibria data, especially in the mafic rocks, provide even tighter constraints on the processes and timescales involved. Most critically, all of the andesites and several of the dacites have ($^{226}Ra/^{230}Th$) > 1, indicating that differentiation to generate some of the silicic magmas in the Katmai system occurred over a much shorter time frame than might be inferred from the U-Th data alone [cf. *Reagan et al.*, 2003]. Overall, there is a general decrease in ($^{226}Ra/^{230}Th$) with the extent of differentiation, as indicated by increasing Th content (Figure 9b). However, the samples with the largest ^{226}Ra-excess are not the basalt or basaltic andesite but the andesites (Table 1), and the biggest increase in the Sr-isotope ratio is between the basalt and the basaltic andesites. Nevertheless, the highest measured values provide a reasonable maximum primary value for the input magmas, since higher ($^{226}Ra/^{230}Th$) ratios have not been observed in any other Aleutian lavas [*George et al.*, 2003]. Therefore, the modeling shown in Figure 9b assumes an initial basaltic magma composition with a ($^{226}Ra/^{230}Th$) ratio of 2.5.

[40] As illustrated in Figure 9b, because both Ra and Th are highly incompatible, closed-system (instantaneous) fractional crystallization has little effect on ($^{226}Ra/^{230}Th$) ratios. Assimilation of older silicic material (assumed to be in secular equilibrium) does result in AFC curves where ($^{226}Ra/^{230}Th$) decreases with increasing Th content, as observed, but these still predict higher ($^{226}Ra/^{230}Th$) ratios than those measured in most of the Katmai samples (Figure 9b). Subsequent mixing with the Naknek sediment could result in a shift below the AFC curves, as observed for many of the samples. However, the effects of the time taken for magmatic evolution are also likely to be important, and more specific constraints implied by the U-series data will be explored subsequently in this paper following a discussion of the thermal budget of the Katmai magmatic system.

7. Numerical Thermal Models

[41] The well-documented volumes of the 1912 eruption, combined with the geochemical and experimental constraints on their depth of origin, afford an excellent opportunity to compare the timescale constraints from a numerical modeling of a cooling magma chamber with those obtained from U-series isotopes. As for the major and trace element modeling, the simplest, end-member model is one in which the 1912 eruption products reflect closed-system differentiation of a magma body into a layered chamber. The minimum volume of this chamber is 13 km^3, but it is highly likely that not all of the magma was erupted. The geochemical modeling presented in this section suggests that it would require some 90% fractionation to produce the rhyolite from the basalt. We therefore model magma volumes ranging from 15 to 65 km^3 encompassing a range in erupted to nonerupted magma ratios of 0 to 5, which is broadly consistent with the findings of *Crisp* [1984].

[42] The way a magma chamber cools reflects a number of processes, including the thermal structure of the surrounding crust, its history of replenishment, the sequence of crystallization, and the chamber shape and way convective processes both within and outside the chamber facilitate redistribution of heat [*Spera*, 1980; *Brandeis and Jaupart*, 1986; *Marsh*, 1988; *Annen et al.*, 2008]. Our objective is not to explore all of the contributory processes, many of which lack adequate constraints (such as the magma supply rate [*Annen et al.*, 2008]). Rather, we are interested in establishing limiting bounds on the cooling of magma chambers of the size appropriate to Katmai.

[43] The thermal budget of a cooling magma chamber is significantly affected by the latent heat released during crystallization, for which our geochemical modeling provides robust constraints, so we aim to establish upper bounds on likely crystallization timescales, explicitly incorporating the crystallization history. We focus our analysis on the cooling of a spherical stagnant magma chamber as a reference case. We also consider the likely effect of different aspect ratios and the role that convective process within the magma chamber may play in accelerating cooling relative to this reference case.

[44] We approximated the MELTS-derived crystallization history using a series of Gaussian functions of the form

$$A^* \exp\left(-(T - T_{trans})^2/dT^2\right)/\sqrt{(\pi \times dT^2)}.$$

Our fit, which deviates from the MELTS model by at most a few degrees (see Figure 8a), has three Gaussian terms, with the parameters listed in Table 4.

[45] A key parameter in the cooling history is the temperature of the surrounding crust. In view of the shallow depths of the magma chamber, between 1 and 5 km and likely 2–3 km [*Hammer et al.*, 2002], we consider a temperature range of 100°C–500°C. The likelihood is that wall rock temperatures were less than 300°C, so we use this as a

Table 4. Parameters Used in Thermal Modeling

Parameter	Value(s) Used
Model symmetry	cylindrical
Model domain size (km)	12.5, 10
Element size (m)	<500
Wallrock temperature (°C)	100 to 500
Magma chamber aspect ratio	1 to 2
Magma chamber volume (km^3)	10 to 65
Thermal conductivity (W/m/K)	3
Density (kg/m^3)	2800
Heat capacity (kJ/kg/K)	1
Latent heat of melting (kj/kg)	400
T intrusion (°C)	1270
A	0.76, 0.16, 0.12
Ttrans (°C)	1270, 1120, 880
dT (°C)	80, 130, 12

reference temperature. We assume constant thermal conductivity with a reference conductivity of 3 W/m/K. Other parameters used in our modeling are listed in Table 4. We consider a range of aspect ratios for ellipsoidal chamber geometries from our reference case of 1 (spherical) to as high as 4, computed in cylindrical coordinates using a direct, symmetric linear solver implemented in COMSOL® with linear, triangular elements and a maximum size of 200 m.

[46] The cooling of a magma chamber depends critically on the rate of internal convection, since convective processes provide more efficient heat transfer from the interior of the magma chamber through the crystallizing walls, maintaining strong temperature gradients near the walls [*Spera*, 1980]. In detail, the way in which the convective heat transfer processes occur is complicated [*Brandeis and Jaupart*, 1986; *Marsh*, 1988]. Here we do not consider the small-scale physical processes that affect convective heat transfer in cooling magmas in detail, but consider the limiting case where vigorous convection is sufficient to effectively homogenize the internal magma chamber temperature up until some critical crystal content, after which there is a rapid transition to conduction-dominated heat transfer. We do so by applying a fictive thermal conductivity related to the degree of crystallization. In the models presented subsequently we consider a threshold of 55% crystallization for the termination of convection, which is likely to be an upper bound. Our objective is to bracket the likely crystallization timescales for a magma chamber: the "reference" case of a stagnant, spherical chamber provides an upper bracket, and the "simulated convection" case provides the lower bracket.

[47] The results shown in Figures 11 and 12 are presented in terms of the degree of crystallization for the entire magma

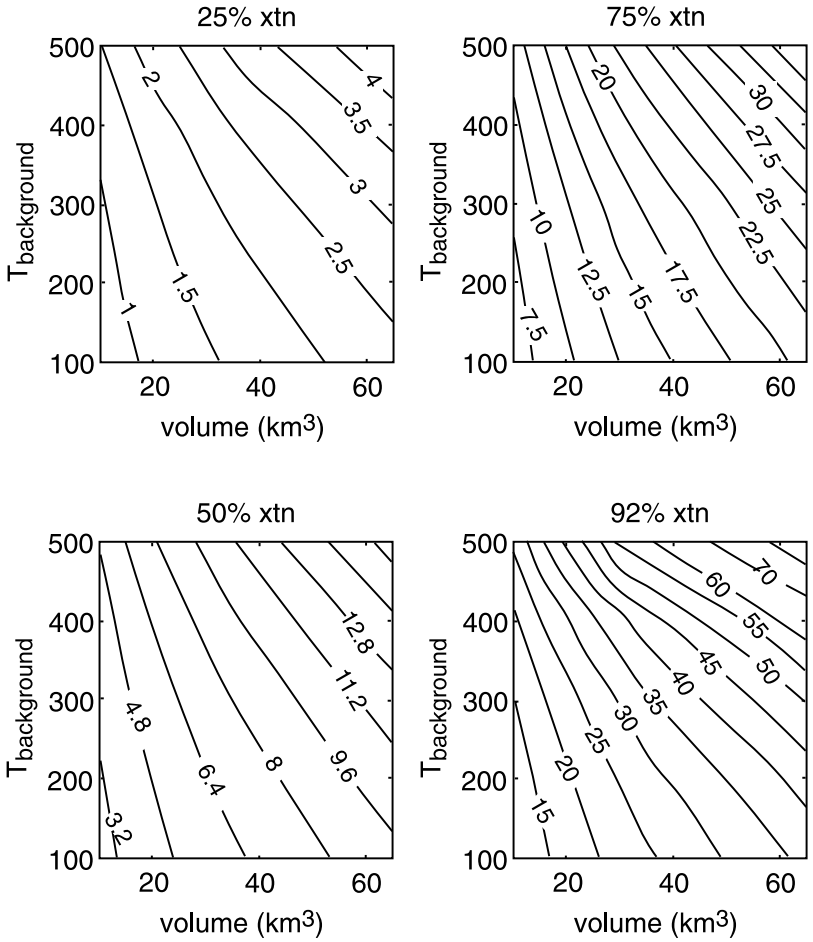

Figure 11. Plots of background (i.e., wall rock) temperature versus magma chamber volume at different extents of crystallization, contoured for time (in kyr) resulting using parameters discussed in the text and Table 4. Model assumes an aspect ratio of 2.

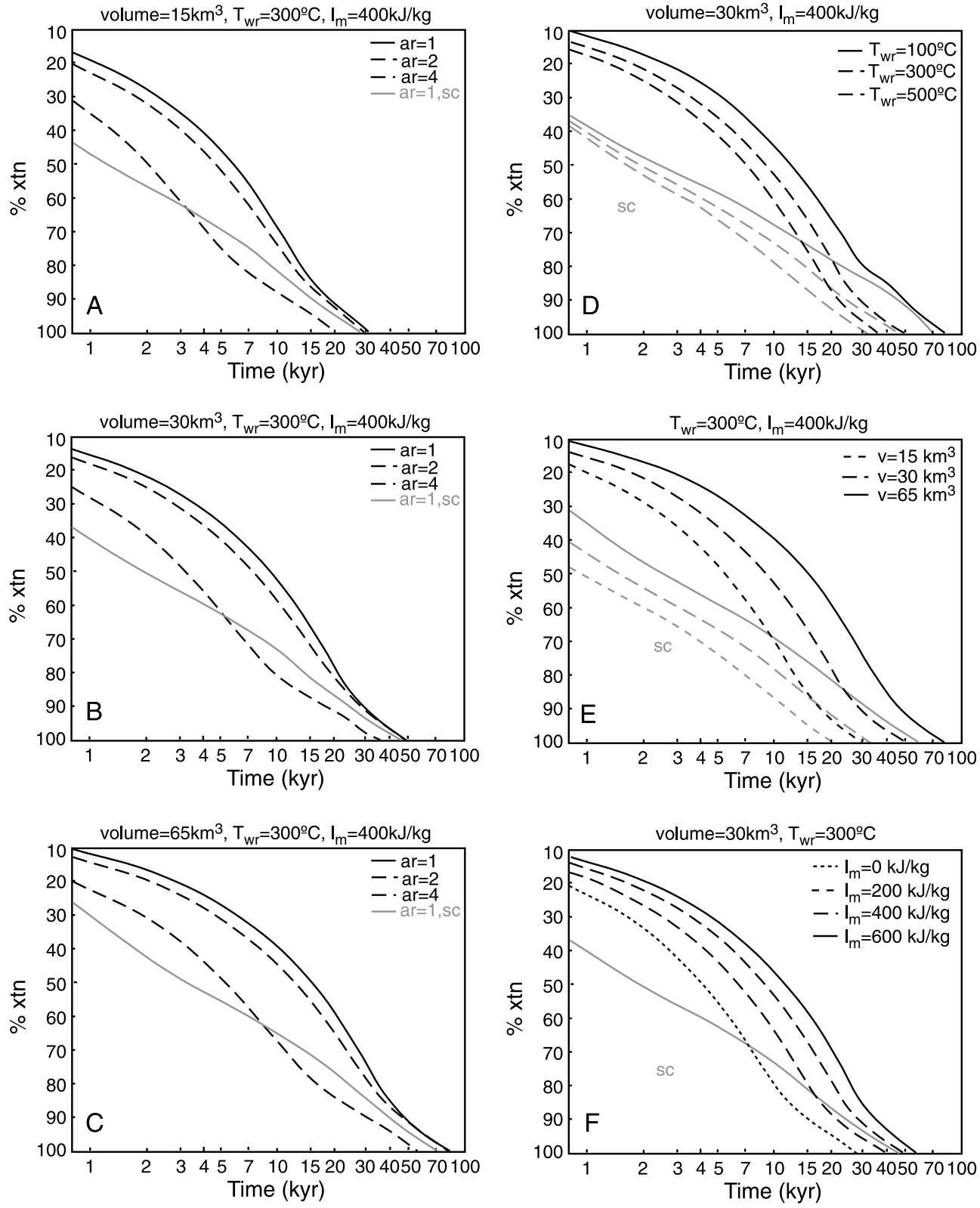

Figure 12. Panels showing the effects of varying key input variables into thermal models such as that presented in Figure 11. (a–c) Varying aspect ratio (labeled "ar") for different magma chamber volume sizes. (d) Varying wall rock temperature for a 30 km^3 chamber. (e) varying chamber volume. (f) Varying latent heat of melting. On all panels the effects of simulated convection (labeled "sc") are indicated by shaded curves.

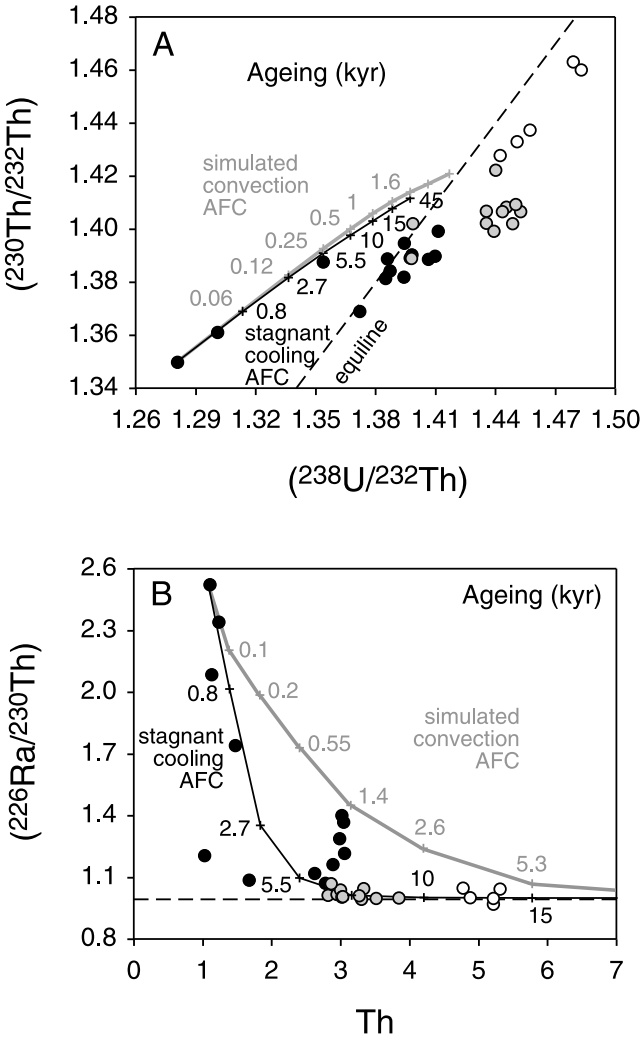

Figure 13. Plots of (a) U-Th equiline diagram. (b) (^{226}Ra/^{230}Th) versus Th showing the results of combining the AFC (rhyolite) and thermal models, assuming the rates of crystallization versus time taken from Figure 12e; the black curves show stagnant convection, shaded curves show simulated convection (time elapsed in kyr).

chamber as a function of time (in kyr), as obtained by integrating over the chamber volume. Figure 11 shows background (i.e., wall rock) temperature versus volume (i.e., total chamber size) at different extents of crystallization, contoured for time for a chamber with an aspect ratio of 2. In Figure 12, we illustrate the relative importance and effects of varying parameters to the model, such as the aspect ratio for different-sized magma chambers (Figures 12a, 12b, and 12c), varying wall rock temperature (Figure 12d), and latent heat of melting (Figure 12f). The gray curves on Figure 12 illustrate the potential importance of the effect of convection, which leads to nearly an order of magnitude decrease in the time required to crystallize up to 50–70% of the magma body. Assuming an aspect ratio of 2, a wall rock temperature of 300°C, latent heat of melting of 400 kJ/kg, and a volume of 65 km^3, Figure 12e shows that it would take ~15 kyr for a magma body of the size inferred to be appropriate for the 1912 eruption to crystallize 50%, and 45 kyr to crystallize 90%. If convection is important, then 50% crystallization could occur in as little as 2.5 kyr, and 90% could occur within 35 kyr (see gray curves in Figure 12e). Note that layered convection would probably be required in order to not destroy the development and preservation of compositional variations.

8. Integration of the Numerical and Geochemical Models

[48] Returning now to the U-series data, we investigate the consequences of implementing the timescales deduced from the thermal models. In Figure 13, the black curves represent the rhyolite AFC model assuming a stagnant 65 km^3 cooling magma chamber from Figure 12e, while the gray curves show the same model assuming a simulated convection model. Since these thermal models take into account the effects of the latent heat of crystallization and convection but do not consider the consequences of heat consumed by partial melting of wall rocks, which is required for assimilation, the timescales for both can be considered as maxima. Importantly, because the time for cooling and crystallization is short compared to the half-life of ^{230}Th (75 kyr) and irrespective of the cooling model assumed, the effect upon the AFC curves in the U-Th equiline diagram is quite restricted (Figure 13a). Thus, U-Th isotopes are probably most sensitive to (variable) parental magma composition and the effects of assimilation. In contrast, the time taken for cooling and crystallization is very significant with respect to the half-life of ^{226}Ra (1.6 kyr), leading to rapid decreases in (^{226}Ra/^{230}Th) that come much closer to simulating the Katmai data. The results show that the data are encompassed by the end-member-scenario thermal models of stagnant and convecting magma chambers (see Figure 13b). In essence, these bracket the likely timescales involved, but there are several observations that add further important detail to the simple time-dependent AFC models just described.

[49] As noted in Section 6, it is likely that the variation in U/Th ratios and Sr isotopes reflects variation in the compositions of the basaltic magmas feeding the system over time. This is supported by the observation that several of the andesites have higher (^{226}Ra/^{230}Th) ratios than either the basalt or basaltic andesite. Assuming that the highest (^{226}Ra/^{230}Th) ratios might be representative of the unmodified mantle signal, this suggests that the andesites probably had crustal residence times of <1000 years. Furthermore, it would appear that the andesites are generally younger (i.e., have higher (^{226}Ra/^{230}Th) ratios) than the dacites (which could be up to ~8000 years old). Because basalt and basaltic andesite would more likely evolve over shorter time periods than the andesites [e.g., *Reagan et al.*, 2003], these basaltic magmas were likely to have evolved from parental magmas that had lower initial (^{226}Ra/^{230}Th) ratios than the andesites. This latter explanation would also suggest that the andesites had the same crustal residence time as the basalt and basaltic andesite, but the data do not allow us to distinguish between these two possibilities.

[50] In contrast, the rhyolites have a (^{226}Ra/^{230}Th) ratio of ~1 and plot at higher (^{230}Th/^{232}Th) than can be achieved by any of the AFC models. This suggests that these are sig-

nificantly older than the other magmas, and this age difference is estimated in Figure 9a to range from ~50–200 kyr [cf. *Jellinek and DePaolo*, 2003]. Importantly, since the thermal models indicate that even the largest likely volume of magma would have solidified in a few tens of kiloyears (see Figures 11 and 12), the rhyolites could not have resided in the upper crust as liquids. Thus, the thermal models also preclude a closed system. Instead, we suggest that they were instead formed by thawing of earlier near-eutectic, silicic materials that produced an aphyric magma. We note that the major and trace element continuity with the associated ejecta nevertheless strongly suggests that any such material was produced from magmas evolving along a similar liquid line of descent.

[51] The overall analysis leads to a preferred model in which the magmatic system was built progressively over time [e.g., *Jellinek and DePaolo*, 2003; *Annen et al.*, 2008] with multiple mafic magma inputs providing both mass and heat, some of which led to thawing of an older, preexisting silicic material that provided much of the magma mass for the rhyolite. These mafic magmas were fluxing the system until shortly before, or at the same time as, the final eruption. We have not attempted to construct a coupled thermal and U-series model of this more complex (but realistic) scenario because there are too many unknown variables for this to be worthwhile at this time. In particular, *Jellinek and DePaolo* [2003] and *Annen et al.* [2008] have shown that the mafic magma supply rate is a critical parameter in such models. This can be estimated for steady state volcanic systems, but clearly Katmai is neither steady state nor typical of the Aleutian arc. Thus, we have little constraint for realistic open-system modeling. Nevertheless, the principal conclusion, that magmas ranging in composition from basalt to rhyolite had a wide range of crustal residence times, appears to be robust.

9. Conclusions

[52] Models invoked to explain the occurrence of large, compositionally zoned volcanic deposits that include significant volumes of rhyolite include long-lived magma chambers that evolved through closed-system fractionation, remelting of silicic plutons, and injection of rhyolite into unrelated andesitic magma chambers. The products of the 1912 Katmai-Novarupta eruption have major and trace element and thermal-redox continuity that is permissive of the first model. However, new Sr and particularly U-series isotope data, along with new thermal models, eliminate the possibility that these ejecta were derived from a closed-system magma chamber. They require variable and minor amounts of assimilation and indicate that the different magma compositions had different crustal residence times. These residence times appear to be not linked to bulk composition in any simple way, and the system most likely was built over time with progressive mafic inputs which continued until shortly before or up until the 1912 eruption. It appears that the rhyolite was dominantly formed by eutectic melting of earlier formed and compositionally related silicic material. There is good evidence that the magmas were not generated in a deep crustal hot zone [cf. *Annen et al.*, 2006], the major and trace element continuity does not support models of interaction of unrelated magmas, and the rhyolite is certainly not younger than the andesite [cf. *Eichelberger and Izbekov*, 2000].

[53] Accordingly, the evidence is that some combination of the first two models is most appropriate, and we envisage the following scenario: the Katmai magmatic system developed over the last few hundred kiloyears, during which time mantle input probably waxed and waned. During periods of increased flux, the magmatic system grew and became stratified, while periods of reduced flux led to greater crystallization. So long as the parental magmas had roughly the same bulk composition and were emplaced under the same pressure-temperature conditions, each batch would be expected to follow the same liquid line of descent. Thus, the major and trace element data mimic closed-system evolution of a single body of magma undergoing internal differentiation. High-silica, near-eutectic liquid at the top of the chamber solidifies but remains close to its solidus, allowing a large amount of rhyolite to be produced with a very small temperature increase. During the final period of increased mantle flux, the system volume grows, the silicic cap melts, and the combination of chamber volume and increasing volatile pressure in the differentiating magmas leads to eruption [cf. *Jellinek and DePaolo*, 2003]. Although this scenario is increasingly envisaged as a common one, it cannot be deduced from field observations or major and trace element compositional variation. Only the short-lived isotope data are sensitive to processes such as protracted magma build-up, differentiation, assimilation, and eruption.

[54] **Acknowledgments.** We wish to thank the organizers of the 2001 Penrose Conference on Longevity and Dynamics of Rhyolitic Magma Systems for inspiration and J. Lowenstern for providing the Naknek sample. We thank J. Blundy and an anonymous reviewer for constructive comments and J. Lowenstern and M. Clynne for internal USGS reviews. This study was supported by NERC grant NER/A/S/2000/01284 and NSF grant EAR0001003 (M.R.) and also used instrumentation funded by ARC LIEF and DEST Systemic Infrastructure Grants, Macquarie University, and industry. S.T. acknowledges the support of the Royal Society University Research Fellowship and subsequently ARC Federation and Professorial Fellowships. Initial analytical work was undertaken by R. George. This is contribution 656 from the Australian Research Council National Key Centre for the Geochemical Evolution and Metallogeny of Continents (http://www.gemoc.mq.edu.au).

References

Annen, C., J. D. Blundy, and R. S. J. Sparks (2006), The genesis of intermediate and silicic magmas in deep crustal hot zones, *J. Petrol.*, *47*, 505–539, doi:10.1093/petrology/egi084.

Annen, C., M. Pichavant, O. Bachmann, and A. Burgisser (2008), Conditions for the growth of a long-lived shallow crustal magma chamber below Mount Pelee volcano (Martinique, Lesser Antilles Arc), *J. Geophys. Res.*, *113*, B07209, doi:10.1029/2007JB005049.

Asimow, P. D., and M. S. Ghiorso (1998), Algorithmic modifications extending MELTS to calculate subsolidus phase relations, *Am. Mineral.*, *83*, 1127–1131.

Bacon, C. R., and T. H. Druitt (1988), Compositional evolution of the zoned calcalkaline magma chamber of Mount Mazama, Crater Lake, Oregon, *Contrib. Mineral. Petrol.*, *98*, 224–256, doi:10.1007/BF00402114.

Blundy, J., and B. Wood (2003), Mineral-melt partitioning of Uranium, Thorium and their daughters, *Rev. Mineral. Geochem.*, *52*, 59–123, doi:10.2113/0520059.

Brandeis, G., and C. Jaupart (1986), On the interaction between convection and crystallization in cooling magma chambers, *Earth Planet. Sci. Lett.*, *77*, 345–361, doi:10.1016/0012-821X(86)90145-7.

Brown, M., and T. Rushmer (2006), *The Differentiation and Evolution of the Continental Crust*, 553 pp., Cambridge Univ. Press, Cambridge, U. K.

Cheng, H., R. L. Edwards, J. Hoff, C. D. Gallup, D. A. Richards, and Y. Asmerom (2000), The half lives of uranium-234 and thorium-230, *Chem. Geol.*, *169*, 17–33, doi:10.1016/S0009-2541(99)00157-6.

Christensen, J. N., and D. J. DePaolo (1993), Time scales of large volume silicic magma systems: Sr isotopic systematics of phenocrysts and glass from the Bishop Tuff, Long Valley, California, *Contrib. Mineral. Petrol.*, *113*, 100–114, doi:10.1007/BF00320834.

Coombs, M. L., and J. E. Gardner (2001), Shallow-storage conditions for the rhyolite of the 1912 eruption at Novarupta, Alaska, *Geology*, *29*, 775–778, doi:10.1130/0091-7613(2001)029<0775:SSCFTR>2.0.CO;2.

Crisp, J. A. (1984), Rates of magma emplacement and volcanic output, *J. Volcanol. Geotherm. Res.*, *20*, 177–211, doi:10.1016/0377-0273(84)90039-8.

Davies, G. R., and A. N. Halliday (1998), Development of the Long Valley rhyolitic magma system: Strontium and neodymium isotope evidence from glasses and individual phenocrysts, *Geochim. Cosmochim. Acta*, *62*, 3561–3574, doi:10.1016/S0016-7037(98)00247-6.

DePaolo, D. J. (1981), Trace element and isotopic effects of combined wall rock assimilation and fractional crystallization, *Earth Planet. Sci. Lett.*, *53*, 189–202, doi:10.1016/0012-821X(81)90153-9.

Eichelberger, J. C., and P. E. Izbekov (2000), Eruption of andesite triggered by dike injection: Contrasting cases at Karymsky volcano, Kamchatka and Mount Katmai, *Philos. Trans. R. Soc. London, Ser. A*, *358*, 1465–1485, doi:10.1098/rsta.2000.0599.

Fabbrizio, A., M. W. Schmidt, D. Gunther, and J. Eikenberg (2009), Experimental determination of Ra mineral/melt partitioning for feldspars and ^{226}Ra-disequilibrium crystallization ages of plagioclase and alkali-feldspar, *Earth Planet. Sci. Lett.*, *280*, 137–148, doi:10.1016/j.epsl.2009.01.022.

Fierstein, J., and W. Hildreth (1992), The plinian eruptions of 1912 at Novarupta, Katmai National Park, Alaska, *Bull. Volcanol.*, *54*, 646–684, doi:10.1007/BF00430778.

Fierstein, J., and C. J. N. Wilson (2005), Assembling an ignimbrite: Compositionally defined eruptive packages in the 1912 Valley of Ten Thousand Smokes ignimbrite, Alaska, *Geol. Soc. Am. Bull.*, *117*, 1094–1107, doi:10.1130/B25621.1.

Fierstein, J., B. F. Houghton, C. J. N. Wilson, and W. Hildreth (1997), Complexities of plinian fall deposition at vent: An example from the 1912 Novarupta eruption (Alaska), *J. Volcanol. Geotherm. Res.*, *76*, 215–227, doi:10.1016/S0377-0273(96)00081-9.

George, R., S. Turner, C. Hawkesworth, J. Morris, C. Nye, J. Ryan, and S.-H. Zheng (2003), Melting processes and fluid and sediment transport rates along the Alaska-Aleutian arc from an integrated U-Th-Ra-Be isotope study, *J. Geophys. Res.*, *108*(B5), 2252, doi:10.1029/2002JB001916.

George, R., S. Turner, C. Hawkesworth, C. Nye, C. Bacon, P. Stelling, and S. Dreher (2004), Chemical versus temporal controls on the evolution of tholeiitic and calc-alkaline magmas at two volcanoes in the Aleutian arc, *J. Petrol.*, *45*, 203–219, doi:10.1093/petrology/egg086.

Ghiorso, M. S., and R. O. Sack (1995), Chemical mass transfer in magmatic processes. IV A revised and internally consistent thermodynamic model for the interpretation and extrapolation of liquid-solid equilibria in magmatic systems at elevated temperatures and pressures, *Contrib. Mineral. Petrol.*, *119*, 197–212, doi:10.1007/BF00307281.

Halliday, A. N., G. A. Mahood, P. Holden, J. M. Metz, T. J. Dempster, and J. P. Davidson (1989), Evidence for long residence times of rhyolitic magma in the Long Valley magmatic system: The isotope record in precaldera lavas of Glass Mountain, *Earth Planet. Sci. Lett.*, *94*, 274–290, doi:10.1016/0012-821X(89)90146-5.

Hammer, J. E., M. J. Rutherford, and W. Hildreth (2002), Magma storage prior to the 1912 eruption at Novarupta, Alaska, *Contrib. Mineral. Petrol.*, *144*, 144–162.

Hawkesworth, C. J., S. Blake, P. Evans, R. Hughes, R. Macdonald, L. E. Thomas, S. P. Turner, and G. Zellmer (2000), The time scales of crystal fractionation in magma chambers: Integrating physical, isotopic, and geochemical perspectives, *J. Petrol.*, *41*, 991–1006, doi:10.1093/petrology/41.7.991.

Hildreth, W. (1981), Gradients in silicis magma chambers: Implications for lithospheric magmatism, *J. Geophys. Res.*, *86*, 10,153–10,192, doi:10.1029/JB086iB11p10153.

Hildreth, W. (1983), The compositionally zoned eruption of 1912 in the Valley of Ten Thousand Smokes, Katmai National Park, Alaska, *J. Volcanol. Geotherm. Res.*, *18*, 1–56, doi:10.1016/0377-0273(83)90003-3.

Hildreth, W., and J. Fierstein (2000), Katmai volcanic cluster and the great eruption of 1912, *Geol. Soc. Am. Bull.*, *112*, 1594–1620, doi:10.1130/0016-7606(2000)112<1594:KVCATG>2.0.CO;2.

Hildreth, W., and C. J. N. Wilson (2007), Compositional zoning of the Bishop Tuff, *J. Petrol.*, *48*, 951–999, doi:10.1093/petrology/egm007.

Huppert, H. E., and R. S. J. Sparks (1988), The generation of granitic magmas by intrusion of basalt into continental crust, *J. Petrol.*, *29*, 599–624.

Jellinek, A. M., and D. J. DePaolo (2003), A model for the origin of large silicic magma chambers: Precursors of caldera-forming eruptions, *Bull. Volcanol.*, *65*, 363–381, doi:10.1007/s00445-003-0277-y.

Kessel, R., M. W. Schmidt, P. Ulmer, and T. Pettke (2005), Trace element signature of subduction-zone fluids, melts and supercritical liquids at 120–180 km depth, *Nature*, *437*, 724–727, doi:10.1038/nature03971.

Klimm, K., J. D. Blundy, and T. H. Green (2008), Trace element partitioning and accessory phase saturation during H_2O-saturated melting of basalt with implications for subduction zone chemical fluxes, *J. Petrol.*, *49*, 523–553, doi:10.1093/petrology/egn001.

Lowenstern, J. B. (1993), Evidence for a copper-bearing fluid in magma erupted at the Valley of Ten Thousand Smokes, Alaska, *Contrib. Mineral. Petrol.*, *114*, 409–421, doi:10.1007/BF01046542.

Lowenstern, J. B., and G. A. Mahood (1991), Petrogenesis of high-silica rhyolite on the Alaska Peninsula, *Geophys. Res. Lett.*, *18*, 1565–1568, doi:10.1029/91GL01554.

Mahood, G. A. (1990), Second reply to comment of R. S. J. Sparks, H. E. Huppert, and C. J.N. Wilson on "Evidence for long residence times of rhyolitic magma in the Long Valley magmatic system: The isotope record in precaldera lavas of Glass Mountain,", *Earth Planet. Sci. Lett.*, *99*, 395–399, doi:10.1016/0012-821X(90)90145-N.

Marsh, B. D. (1988), On convective style and vigor in sheet-like magma chambers, *J. Petrol.*, *30*, 479–530.

Miller, S., D. S. Burnett, P. D. Asmow, D. L. Phinney, and I. D. Hutcheon (2007), Experimental study of radium partitioning between anorthite and melt at 1 atm, *Am. Mineral.*, *92*, 1535–1538, doi:10.2138/am.2007.2640.

Oldenburg, C., F. Spera, D. Yuen, and G. Sewell (1989), Dynamic mixing in magma bodies: Theory, simulations, and implications, *J. Geophys. Res.*, *94*, 9215–9236, doi:10.1029/JB094iB07p09215.

Plank, T., L. B. Cooper, and C. E. Manning (2009), Emerging geothermometers for estimating slab surface temperatures, *Nat. Geosci.*, *2*, 611–615, doi:10.1038/ngeo614.

Price, R. C., J. A. Gamble, I. E. M. Smith, R. B. Stewart, S. Eggins, and I. C. Wright (2005), An integrated model for the temporal evolution of andesites and rhyolites and crustal development in New Zealand's North Island, *J. Volcanol. Geotherm. Res.*, *140*, 1–24, doi:10.1016/j.jvolgeores.2004.07.013.

Prowatke, S., and S. Klemme (2006), Trace element partitioning between apatite and silicate melts, *Geochim. Cosmochim. Acta*, *70*, 4513–4527, doi:10.1016/j.gca.2006.06.162.

Rampino, M. R., and S. Self (1984), Sulphur-rich volcanic eruptions and stratospheric aerosols, *Nature*, *310*, 677–679, doi:10.1038/310677a0.

Reagan, M. K., K. W. W. Sims, J. Erich, R. B. Thomas, H. Cheng, R. L. Edwards, G. Layne, and L. Ball (2003), Time-scales of differentiation from mafic parents to rhyolite in North American continental arcs, *J. Petrol.*, *44*, 1703–1726, doi:10.1093/petrology/egg057.

Reubi, O., and J. Blundy (2009), A dearth of intermediate melts at subduction zone volcanoes and the petrogenesis of arc andesites, *Nature*, *461*, 1269–1273, doi:10.1038/nature08510.

Robock, A., and J. Mao (1992), Winter warming from large volcanic eruptions, *Geophys. Res. Lett.*, *19*, 2405–2408, doi:10.1029/92GL02627.

Rollinson, H. (1993), *Using Geochemical Data: Evaluation, Presentation, Interpretation*, 352 pp., Longman, Harlow, U. K.

Sims, K. W., et al. (2008), An interlaboratory assessment of the Th isotopic composition of synthetic and rock standards, *Geostand. Geoanal. Res.*, *32*, 65–91, doi:10.1111/j.1751-908X.2008.00870.x.

Sparks, R. S. J., H. E. Huppert, and C. J. N. Wilson (1990), Comment on "Evidence for long residence times of rhyolitic magma in the Long Valley magmatic system: The isotope record in precaldera lavas of Glass Mountain" by A. N. Halliday, G. A. Mahood, P. Holden, J. M. Metz, T. J. Dempster and J. P. Davidson (1990), *Earth Planet. Sci. Lett.*, *99*, 387–389, doi:10.1016/0012-821X(90)90143-L.

Spera, F. J. (1980), Thermal evolution of plutons: A parameterised approach, *Science*, *207*, 299–301, doi:10.1126/science.207.4428.299.

Trial, A. F., and F. J. Spera (1990), Mechanisms for the generation of compositional heterogeneities in magma chambers, *Geol. Soc. Am. Bull.*, *102*, 353–367, doi:10.1130/0016-7606(1990)102<0353:MFTGOC>2.3.CO;2.

Turner, J. S., and I. H. Campbell (1986), Convection and mixing in magma chambers, *Earth Sci. Rev.*, *23*, 255–352, doi:10.1016/0012-8252(86)90015-2.

Turner, S., B. Bourdon, and J. Gill (2003), Insights into magma genesis at convergent margins from U-series isotopes, *Rev. Mineral. Geochem.*, *52*, 255–315, doi:10.2113/0520255.

Turner, S., S. Black, and K. Berlo (2004), ^{210}Pb–^{226}Ra and ^{232}Th–^{228}Ra systematics in young arc lavas: Implications for magma degassing and ascent rates, *Earth Planet. Sci. Lett.*, *227*, 1–16, doi:10.1016/j.epsl.2004.08.017.

van den Bogaard, P., and C. Schirnick (1995), ^{40}Ar/^{39}Ar laser probe ages of Bishop Tuff quartz phenocrysts substantiate long-lived silicic magma chamber at Long Valley, U.S, *Geology*, *23*, 759–762, doi:10.1130/0091-7613(1995)023<0759:AALPAO>2.3.CO;2.

Ward, P. L., A. M. Pitt, and E. Endo (1991), Seismic evidence for magma in the vicinity of Mt. Katmai, Alaska, *Geophys. Res. Lett.*, *18*, 1537–1540, doi:10.1029/91GL01906.

Watson, E. B., and T. M. Harrison (1983), Zircon saturation revisited: Temperature and composition effects in a variety of crustal magma types, *Earth Planet. Sci. Lett.*, *64*, 295–304, doi:10.1016/0012-821X(83)90211-X.

Westrich, H. R., J. C. Eichelberger, and R. L. Hervig (1991), Degassing of the 1912 Katmai magmas, *Geophys. Res. Lett.*, *18*, 1561–1564, doi:10.1029/91GL01667.

Wolff, J. A., G. Wörner, and S. Blake (1990), Gradients in physical parameters in zoned felsic magma bodies: Implications for evolution and eruptive withdrawal, *J. Volcanol. Geotherm. Res.*, *43*, 37–55, doi:10.1016/0377-0273(90)90043-F.

Wood, B., and J. Blundy (1997), A predictive model for rare earth element partitioning between clinopyroxene and anhydrous silicate melt, *Contrib. Mineral. Petrol.*, *129*, 166–181, doi:10.1007/s004100050330.

C. Hawkesworth, Department of Earth Sciences, University of Bristol, Wills Memorial Building, Queen's Road, Bristol BS8 1RJ, UK.

W. Hildreth, United States Geological Survey, 345 Middlefield Rd., Menlo Park, CA 94025, USA.

M. Reagan, Department of Geoscience, University of Iowa, Trowbridge Hall, N. Capitol St., Iowa City, IA 52242 USA.

M. Sandiford, School of Earth Sciences, University of Melbourne, Parkville, VIC 3010, Australia.

S. Turner, GEMOC, Department of Earth and Planetary Sciences, Macquarie University, North Ryde, NSW 2109, Australia. (simon.turner@mq.edu.au)